Precambrian Research 379 (2022) 106801

Contents lists available at ScienceDirect

Precambrian Research

journal homepage: www.elsevier.com/locate/precamres

Carbonatitic footprints in the Bayan Obo REEs deposit as seen from pyrite geochemistry

Hai-Dong She [a,b], Hong-Rui Fan [a,b,c,d,*], Kui-Feng Yang [a,b,c,d], Xuan Liu [e], Xing-Hui Li [a,c], Zhi-Hui Dai [f]

[a] Key Laboratory of Mineral Resources, Institute of Geology and Geophysics, Chinese Academy of Sciences, Beijing 100029, China
[b] College of Earth and Planetary Sciences, University of Chinese Academy of Sciences, Beijing 100049, China
[c] Innovation Academy for Earth Science, Chinese Academy of Sciences, Beijing 1000029, China
[d] State Key Laboratory of Baiyunobo Rare Earth Resource Researches and Comprehensive Utilization, Baotou Research Institute of Rare Earths, Baotou 014030, China
[e] Geological Survey of Finland, P.O. Box 96, FI-02151 Espoo, Finland
[f] State Key Laboratory of Deposit Geochemistry, Institute of Geochemistry, Chinese Academy of Sciences, Guiyang 550081, China

ARTICLE INFO

Keywords:
Pyrite
Trace element
Sulfur isotope
Bayan Obo
China

ABSTRACT

The genesis of the Bayan Obo REEs deposit has been debated for a century. The most outstanding issue concerns the genesis of the ore-hosting dolomite and the contribution of the Paleozoic overprint events in the rare earth budget. Pyrite offers a unique window into those debates in that it is the only common fingerprinting mineral shared by both events. In this contribution, LA-ICP-MS trace element mapping, *in-situ* elemental and sulfur isotopic analyses on pyrite are integrated in order to constrain the genesis of ore-hosting dolomite and evaluate the contribution of the Paleozoic thermal events to enormous REEs resources. Five types of pyrite were distinguished in ore-hosting dolomites, various types of ore and skarns based on mineral paragenesis and geochemical signatures. The dolomites contain early euhedral pyrite (Py-1) overgrown by magnetite and euhedral pyrite (Py-2w in the West Open Pit and Py-2d in the deep boreholes) associated with pyrrhotite, monazite, dolomite and apatite. By contrast, pyrite in the banded ores (Py-3b) and the massive ores (Py-3 m) was co-precipitated with magnetite, aegirine, fluorite, riebeckite, REEs minerals and apatite. Pyrite in the vein ores (Py-4) usually coexists with barite, quartz, aegirine and calcite, and those (Py-5) in skarns associated with biotite and amphibole. Py-1 is enriched in Ti, Ni, Nb, Hf and REEs, with high Co/Ni and Y/Ho ratios (ca. 66), and high $\delta^{34}S$ values from +8.6‰ to +13.8‰. In comparison, Py-2w and Py-2d have higher Co/Ni yet lower Y/Ho (ca. 11) ratios, but exhibit magmatic $\delta^{34}S$ values (-1.0‰ to +3.0‰; −1.0‰ to +3.7‰). Py-3b and Py-3 m are relatively enriched in Cr, Mn, Zn and LREEs, and possess intermediate $\delta^{34}S$ values (+5.7‰ to +7.7‰, and +0.2‰ to +2.4‰, respectively). Py-4 is generally depleted in trace elements with magmatic $\delta^{34}S$ values (-2.0‰ to +2.7‰). Compared with Py-3 m and Py-3b, Py-5 is characterized by high Co yet low Ti, Cr, Mn, Cu and Zn with variable REEs, and is enriched in ^{34}S ($\delta^{34}S$: +9.1‰ to +10.8‰). The high $\delta^{34}S$ value and Y/Ho ratio in Py-1 indicate that the ore-hosting dolomite is an igneous carbonatite originated from partial melting of upper mantle contaminated by altered and subducted oceanic crust. The marked difference in trace elements and sulfur isotopes between Py-3, Py-4 and Py-5 implies that the Paleozoic thermal events contributed little to the primary REEs mineralization except remobilizing preexisting ore metals.

1. Introduction

The Bayan Obo REEs deposit, the dominant supplier of rare earth metals of the world, has been attracting attention from all walks of life due to its enormous reserves of LREEs, Nb, Fe and Sc metals. Since being first found in 1927 as an iron deposit by Mr. Daoheng Ding, extensive research work has been conducted regarding its mineralogical and geochemical characteristics. Recently, *in-situ* microanalyses have greatly improved the understanding of the genesis of this giant deposit (Campbell et al., 2014; Fan et al., 2014; Ling et al., 2014; Lai et al., 2016; Zhang et al., 2017; Song et al., 2018; Yang et al., 2011, 2019; Chen et al., 2020; Liu et al., 2018a, 2020; Li et al., 2021a; She et al., 2021).

* Corresponding author at: Key Laboratory of Mineral Resources, Institute of Geology and Geophysics, Chinese Academy of Sciences, Beijing 100029, China.
E-mail address: fanhr@mail.iggcas.ac.cn (H.-R. Fan).

https://doi.org/10.1016/j.precamres.2022.106801
Received 21 September 2021; Received in revised form 29 June 2022; Accepted 15 July 2022
Available online 28 July 2022

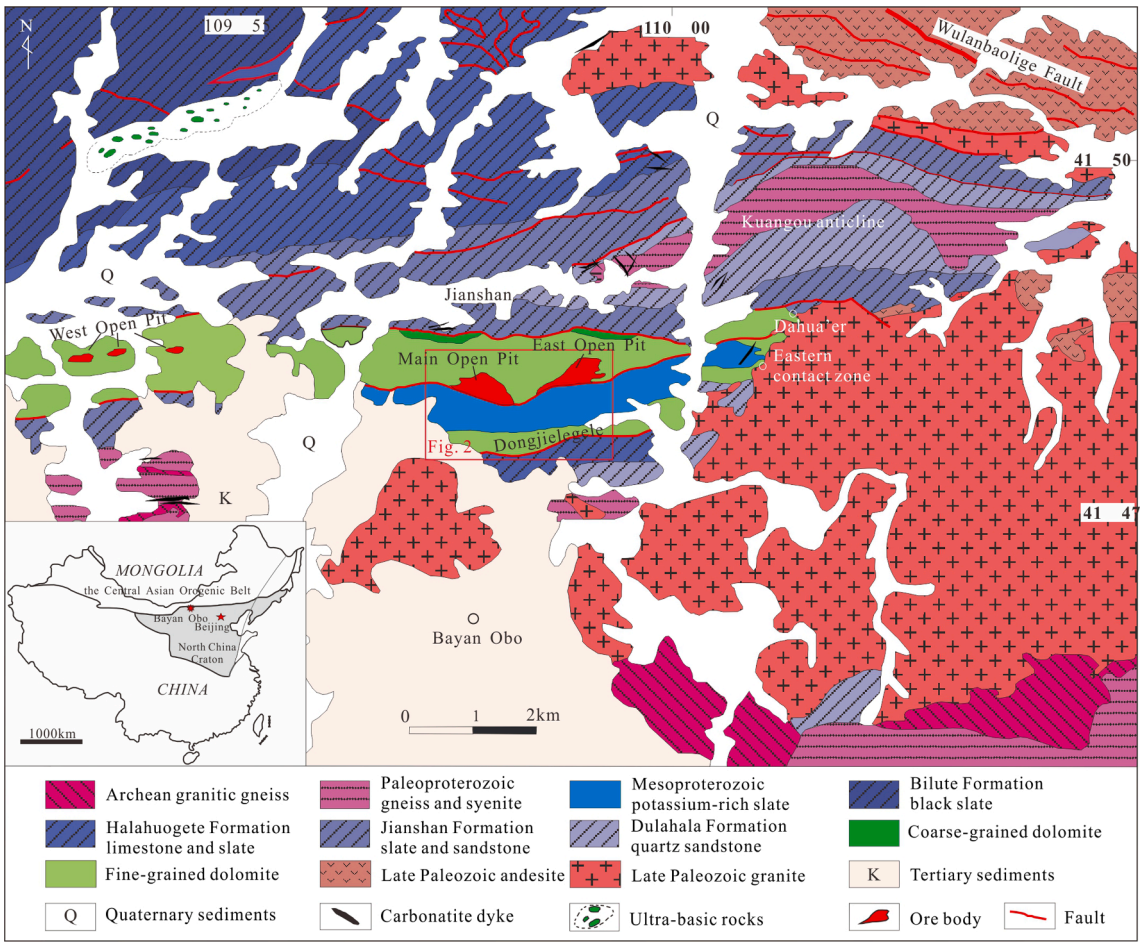

Fig. 1. Geographic location map and Geological sketch map [revised from Yang et al., (2011)] of the Bayan Obo REEs-Nb-Fe deposit.

Nonetheless, the origin of the ore-hosting dolomite is still under debate. One school of thought advocates that the dolomite (named as H_8 dolomite) forms a layer of the regional rift-related sedimentary sequence referred to as the Bayan Obo Group based on field occurrence, paleontology and geochemistry (Meng, 1982; Wang et al., 1994; Qin et al., 2007; Yang et al., 2009). In contrast, the other one favors the idea of igneous carbonatite that intruded into the Bayan Obo Group based on the mineralogy, geochemistry and contact relationship between the ore-hosting dolomite and surrounding sedimentary formations (Le Bas et al., 1997; Sun et al., 2013; Campbell et al., 2014; Fan et al., 2016; Song et al., 2018; Yang et al., 2011, 2019). Therefore, there are various schools of thought and still no consensus on this issue.

In addition, there also has been a fierce controversy over the ore-forming time of Bayan Obo deposit in the past three decades (Wang et al., 1994; Chao et al., 1997; Zhang et al., 2003; Liu et al., 2004; Hu et al., 2009; Fan et al., 2014; Zhang et al., 2017; Yang et al., 2011, 2019; Li et al., 2021a), but recently a consensus has been reached that the main metallogenic event that formed a large amount of REEs budgets occurred in Mesoproterozoic (1.4–1.2 Ga; Campbell et al., 2014; Zhu et al., 2015; Fan et al., 2016; Yang et al., 2017; Li et al., 2021a, 2021b). The Bayan Obo area was strongly re-worked by multiple thermal events after main mineralization, and the Caledonian vein mineralization (ca. 440 Ma) and Hercynian granite intrusion events (ca. 270 Ma) are the most important ones (Yang et al., 2007; Fan et al., 2009; Hu et al., 2009; Campbell et al., 2014; Ling et al., 2014). They are the response to the ocean-continent subduction and the continent–continent collision events in the Bayan Obo area during the closure of the Paleo Asian Ocean (Tang, 1990; Wang et al., 1994; Chao et al., 1997; Xiao et al., 2003; Li, 2006), and formed coarse-grained rare earth minerals and irregular skarn iron ore bodies, respectively (Yang et al., 2007; Hu et al., 2009). Although the mineralization and overprinting processes in the Bayan Obo deposit have been clarified in time sequence, the role of these two reworking events in accumulating REEs budgets remains unclear. Notably, significant amounts of pyrite are present at Bayan Obo, most of which are distributed in vein form, and a small amount is disseminated distributed in ore-hosting dolomites and REEs-Fe ores. Pyrite has been long thought as an important manifestation of the Paleozoic event (IGCAS, 1988), even though, field occurrence and microstructure characteristics seem to indicate a *trans*-event feature. For instance, the fine euhedral pyrite in the ore-hosting dolomite was totally different from those in vein ores in morphology and mineral association. Therefore, a detailed examination of pyrite is needed to determine whether the source of the sulfur is only Paleozoic vein mineralization.

Pyrite, FeS_2, the most common sulfide in the crust, is extensively distributed in various geological bodies related to magmatic, hydrothermal, sedimentary and metamorphic events, or biological activity (Craig and Vokes, 1993; Clark et al., 2004; Zhao and Jiang, 2007; Chandra and Gerson, 2010), especially in sulfide related deposits (Zheng et al., 2013; Jin et al., 2015; Belousov et al., 2016). The characteristics of pyrite morphology and chemical composition, especially trace element composition, have specific genetic significance, and can provide constraints on the formation environment of pyrite. In addition to the essential components Fe and S, natural pyrite also contains abundant trace elements in the forms of micro-inclusions (Cu, Zn, Pb, Ba, Bi, Ag and Sb), non-stoichiometric substitutions (As, Tl, Au and Mo) and stoichiometric substitutions (Co, Ni, Se and Te; Huston et al., 1995; Abraitis et al., 2004; Large et al., 2007; Deditius et al., 2011). The accumulated data of trace elements in pyrite shows that there are obvious differences

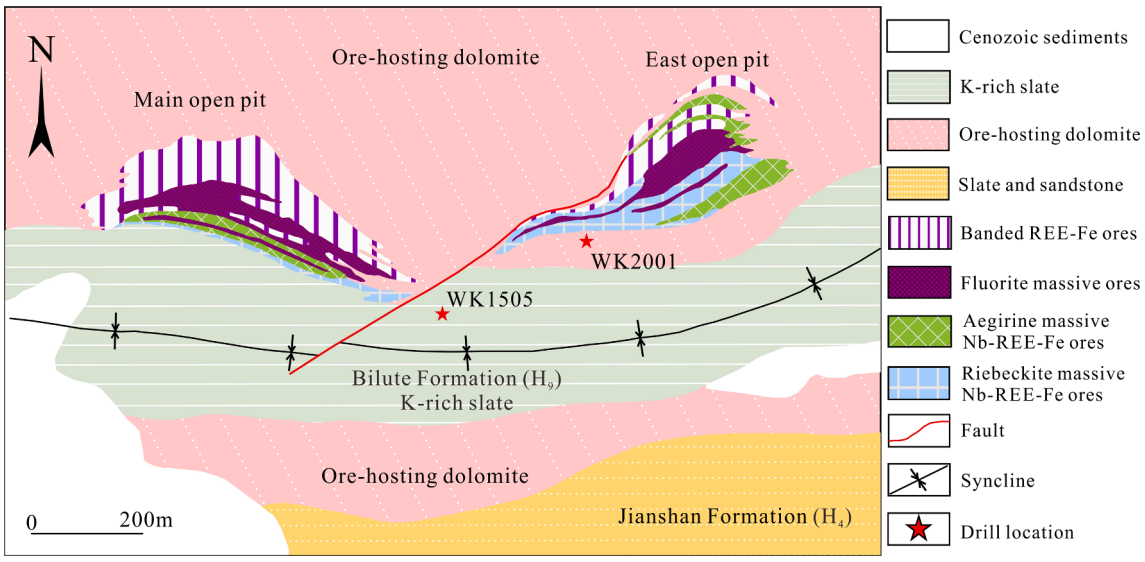

Fig. 2. Geological sketch and mineralization zoning map of Main and East ore-bodies at Bayan Obo. Modified from IGCAS (1988) and Liu et al., (2018a).

in the degree of substitution of Fe and S in pyrite formed in the different geological environments (Price, 1972; Bralia et al., 1979; Maslennikov et al., 2009; Deditius et al., 2011; de Ronde et al., 2011; Gregory et al., 2019). Thus, the trace components in pyrite can provide important indicative information about the deposition environment, petrogenesis, metallogenic process and environmental evolution. Since the 1970s, sufficient geological studies have been conducted based on the characteristic trace element content and ratios (e.g. Co/Ni, S/Se, Se/Te) of pyrite, covering studies of petrology, metallogeny and paleo-environment reconstruction (Loftus-Hills and Solomon, 1967; Brill, 1989; Raymond, 1996; Clark et al., 2004; Monteiro et al., 2008; Agangi et al., 2014; Large et al., 2014; Gregory et al., 2015; Meng et al., 2019; Mukherjee and Large, 2020). In addition, the sulfur isotopic compositions of pyrite with different geological backgrounds are also very different. For example, the sulfur isotopic composition of igneous rocks is similar to that of meteorites, with a small range of variation, and $\delta^{34}S$ is about 0 ± 2‰ (Nielsen, 1979; Seal, 2006). In contrast, the sulfur isotopic composition of sedimentary rocks varies greatly, with large range of −40‰ to +50‰ (Nielsen, 1979; Ohmoto, 1972; Ohmoto and Rye, 1979; Ohmoto and Goldhaber, 1997; Seal, 2006; Hoefs, 2015). Therefore, the sulfur isotope data combined with geological and mineralogical data of the deposit can be used to constrain the physico-chemical condition (T, fO_2, fS_2, $m_{\sum S}$) and origin ($\delta S^{34}_{\sum S}$) of ore-forming fluids, as well as the ore precipitation mechanism (Ohmoto, 1972; Reich et al., 2005; Drüppel et al., 2006; Nikiforov et al. 2006; Hodkiewicz et al., 2009; Su et al. 2012; Tanner et al., 2016; Li et al., 2018; Feng et al., 2020; Hu et al., 2020). Compared with most other common sulfides, pyrite keeps stable under various physicochemical conditions, exhibiting refractory behaviour to post-depositional metamorphism (Craig and Vokes, 1993; Craig et al., 1998; Agangi et al., 2013). Therefore, the geological records before metamorphism are more or less preserved, which are important "mineral probe" for the study of geological events before or during metamorphism. Moreover, its universality makes it very suitable for the microscopic analysis of metallogenic process reconstructed by space and time (Agangi et al., 2013; Keith et al., 2016).

As yet, little attention is paid to trace elements and sulfur isotopes of sulfide in the Bayan Obo deposit (Cao et al., 1994; Lai and Yang, 2013; Liu et al., 2018a), which may provide unique footprints of the deposit genesis. This contribution presents first-hand trace elements and sulfur isotope data on pyrite in ore-hosting dolomite, ore, and skarn, with which it is attempted to shed new light on the genesis of ore-hosting dolomite and role of the Paleozoic thermal events for REEs mineralization at Bayan Obo.

2. Geologic background and sampling

2.1. Archean-mesoproterozoic sequences

The Bayan Obo REEs deposit is located in the northern margin of the North China Craton and adjacent to the Central Asian Orogenic Belt in the north (Fig. 1). The primary fault in the area is Wulanbaolige deep fault, also known as the Bayan Obo-Chifeng fault, located about 10 km to the north of the Bayan Obo mining area. The subordinate fault is Baiyinjiaolake-Bayan Obo fault, the eastern part of which is also known as the east–west Kuangou fault cut off by the Wulanbaolige fault. The basement rock in the mining area is composed of the Archean granitic-gneiss distributed in the southeast of the mining area, the Paleoproterozoic gneiss and syenite in the core of Kuangou anticline and the south of the Main Open Pit, and the late Paleoproterozoic garnet-bearing gneiss in the south of the East Open Pit (Fan et al., 2010).

The Paleoproterozoic-Mesoproterozoic Bayan Obo Group, nearly 10 km thick weak-metamorphic sedimentary sequence (clastic-shale-carbonated), un-conformably overlies the metamorphic basement (Fig. 1). These rocks are widely distributed in the two limbs of the Kuangou anticline, and show obvious deformational and metamorphic characteristics. Those on the southern limb have undergone intense thermal event transformation with high degree of metamorphism, while those on the northern limb are devoid of deformation (IGCAS, 1988). The Bayan Obo Group is divided into six formations (Dulahala, Jianshan, Halahuogete, Bilute, Baiyinbaolage and Hujiertu), consisting of eighteen unites. It was deposited in Paleoproterozoic to Mesoproterozoic based on radiometric dating (carbonate ^{207}Pb-^{206}Pb isochron age 1649 ± 45 Ma, Yang et al., 2012; detrital zircon U-Pb ages for the Dulahaala Formation and Jianshan Formation, maximum deposition ages of 1822 ± 9 Ma and 1710 ± 29 Ma, respectively, Zhong et al., 2015; Pb-Pb age of the Halahuogete Formation limestone of 1619 ± 150 Ma, Lai et al., 2016; detrital zircon U-Pb ages for the Dulahala-Jianshan Formation, Bilute Formation and Baiyinbaolage Formation of 1.81–1.7 Ga, 1.58–1.35 Ga and 1.25–1.0 Ga, respectively, Zhou et al., 2018).

2.2. Paleozoic sequences

The region comprises a large area of Paleozoic granitoids (including granodiorite, monzogranite, and biotite granite), mainly distributed in the southeast of the East Open Pit and the south of the West Open Pit.

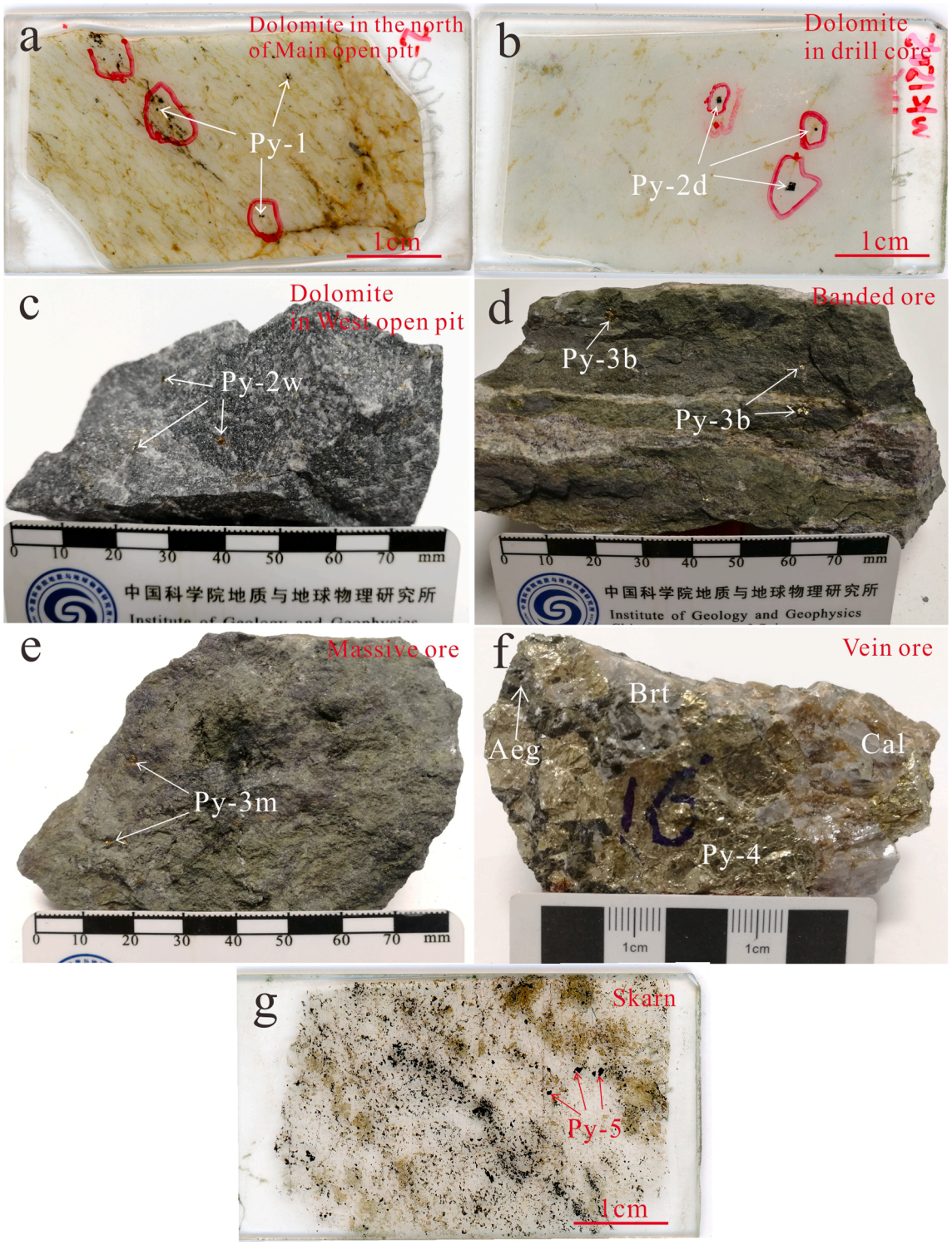

Fig. 3. Pyrite grains in different types of rocks and ores. **a:** Disseminated pyrite in ore-hosting dolomite, the edge of which is metasomatized by magnetite; **b:** Disseminated pyrite in ore-hosting dolomite in deep boreholes of Main and East Open Pits, often associated with pyrrhotite; **c:** Disseminated pyrite in ore hosting dolomite of West Open Pit; **d:** Pyrite in banded REEs-Nb-Fe ores; **e:** Pyrite in massive REEs-Fe ores; **f:** Coarse-grained pyrite in Paleozoic vein ores; **g:** Disseminated pyrite in Eastern Contact Zone skarn. Aeg: aegirine; Brt: barite; Cal: calcite; Py: pyrite.

They were formed at 281–263 Ma (peaking at 270 Ma) according to compilation of geochronological constraints (Fan et al., 2009), in a geodynamic setting related to the continent–continent collision in the late stage of Paleo-Asian Ocean closure (Wang et al., 1994; Chao et al., 1997; Xiao et al., 2003). There also exist slightly earlier gabbro and diorite intrusions (Bai et al., 1996; IGCAS, 1988). Most of them intruded into the stratum as stocks or dikes, which are crosscut or enclosed as enclaves by the granitoids.

2.3. Ore deposit geology

The Bayan Obo REEs (-Nb-Fe) deposit hosts 57.4 Mt REE_2O_3 ores at

an average grade of 6%, 2.16 Mt Nb_2O_5 ores at an average grade of 0.13%, and >1500 Mt iron ores at an average grade of 35% (Drew et al., 1990; Chao et al., 1997; Hao et al., 2002). The REEs-Nb orebodies are located near the intersection between the Wulanbaolige and Kuangou faults. The main structure is the Kuangou anticline on the north side of the open pits, which is nearly east–west in the axis and inclines westward. The strata on both limbs of the anticline are the Mesoproterozoic Bayan Obo Group. The deposit is currently under exploitation in the East Open Pit, Main Open Pit and West Open Pit gradually merged by dozens of small mines (Fig. 1). The ore bodies are lenticular, strike nearly E-W and incline southward, and are hosted in a set of nearly EW-trending dolomites, which are further divided into north and south parts by the H_9 K-rich slate of the Bilute formation. The alkaline hydrothermal metasomatism of the Main and East ore bodies is intense, mainly consisting of a set of alkaline mineral assemblage represented by aegirine and sodium-amphibole. Corresponding types of ores to the alteration zonation generally includes dolomite-dominated REEs-Nb-Fe ore, banded REEs-Nb-Fe ore, massive fluorite-rich Fe ore, massive aegirine-rich REEs-Nb-Fe ore and massive Na-amphibole-rich REEs-Nb-Fe ore (Fig. 2; IGCAS, 1988). The main rare earth minerals are monazite, bastnäsite, parisite, cebaite, huanghoite, and etc. The Nb-bearing minerals are mainly fergusonite-(Y), columbite, aeschynite, pyrochlore and baotite, and the Fe ore minerals are magnetite and hematite (Chao et al., 1991; Fan et al., 2016; She et al., 2021).

2.4. Sampling strategy

Pyrite-bearing rock samples are collected in the Bayan Obo area to cover all possible rock types and areas. These samples fall into four categories: (1) ore-hosting dolomite containing disseminated pyrite from the north of the Main Open Pit (Fig. 3a), deep boreholes outside the Main Open Pit (Fig. 3b; boreholes No. WK1505 and WK2001) and the West Open Pit (Fig. 3c; 1440 and 1510 m level), with main minerals are dolomite, apatite and monazite; (2) banded ores from the Main Open Pit (Fig. 3d; 1458 m level) and massive ores from the East Open Pit (Fig. 3e; 1348 m and 1362 m levels), both containing most of the rare earth and iron resources of the deposit, and the main minerals are magnetite, fluorite, bastnäsite, aegirine, monazite, riebeckite and apatite; (3) coarse-grained vein ores from the Main Open Pit (Fig. 3f; 1444 m level), this kind of ore is mainly distributed in the shallow part of the Main and East Open Pits, and the main minerals are pyrite, barite, aegirine and calcite; (4) skarn in the eastern contact zone (Fig. 3g), which is the product of the Hercynian granite emplacement event, and its main composition minerals are plagioclase, biotite, amphibole and albite. The detailed drill locations can refer to Fig. 2. Pyrites and its host rock petrography are described in detail below.

3. Analytical methods

3.1. LA-ICP-MS trace element analysis and mapping

In-situ trace element and sulfur isotope analyses are made on thin section. Selection of laser spots were guided with petrographic microscope to avoid surface contaminations, fractures, and mineral inclusions. Trace element analyses of pyrite were conducted with an Agilent 7700x quadrupole ICP-MS coupled to an ASI RESOLution-LR-S155 laser microprobe equipped with a Coherent Compex-Pro 193 nm ArF excimer laser at the State Key Laboratory of Ore Deposit Geochemistry, Institute of Geochemistry, Chinese Academy of Sciences (IGCAS). During ablation, the sample chamber was purged with Ar gas (900 mL/min), and then the ablated material was transported by He gas (350 mL/min). Each analysis consists of approximately 30 s of background acquisition (gas blank), followed by 60 s of data collection from the sample. The analysis was carried out with the following laser parameters: 26 μm beam size, 5 Hz pulse frequency and 3 J/cm^2 energy intensity. A total of 35 elements were analyzed using isotopes ^{45}Sc, ^{49}Ti, ^{51}V, ^{53}Cr, ^{55}Mn, ^{57}Fe, ^{59}Co, ^{60}Ni, ^{65}Cu, ^{66}Zn, ^{71}Ga, ^{72}Ge, ^{85}Rb, ^{88}Sr, ^{89}Y, ^{93}Nb, ^{115}In, ^{137}Ba, ^{139}La, ^{140}Ce, ^{141}Pr, ^{143}Nd, ^{147}Sm, ^{151}Eu, ^{155}Gd, ^{159}Tb, ^{163}Dy, ^{165}Ho, ^{166}Er, ^{169}Tm, ^{173}Yb, ^{175}Lu, ^{179}Hf, ^{232}Th and ^{238}U. The internal standard Peru Py was used to calibrate the concentration of S and Fe. GSE-1G and GSD-1G were used to convert the integrated count data into the concentrations for lithophile elements (Sc, Ti, Cr, Mn, Y, Nb, REEs, Hf and Th), and STDGL3 for chalcophile and siderophile elements (Co, Ni, Cu, Zn and Ge; Danyushevsky et al., 2011). The preferred element concentration values for USGS reference glasses are from the GeoReM database (https://georem.mpch-mainz.gwdg.de/). The sulfide reference material MASS-1 was analyzed as an unknown sample to check the accuracy of the analysis (Wilson et al., 2002). Compared with the preferred values, the analytical errors were mainly within ±10% (Supplementary Table 1). ICPMSDataCal was used to select and integrate the background signal and analyte signal off-line, as well as time-drift correction and quantitative calibration (Liu et al., 2008).

Trace element mapping of pyrite was also performed with the same setup. A set of touching parallel lines arranged in a grid (typically 60*60) was ablated using a beam size of 7 μm with a rastering speed of 7 μm/s. A group of thirteen elements was chose for image analysis (^{137}Ba, ^{140}Ce, ^{59}Co, ^{53}Cr, ^{163}Dy, ^{57}Fe, ^{139}La, ^{175}Lu, ^{93}Nb, ^{143}Nd, ^{60}Ni, ^{88}Sr, ^{89}Y). Acquisition time was set to 0.002 s for most elements with a total scanning time of ~0.2 s. Before collecting the signal, the same beam spot as the test signal and the scanning speed of 20 μm/s was used for pre-stripping, so as to reduce surface contamination. Sulfide mapping was triggered and ended with two lines of ablation of STDGL3, GSE-1G and GSD-1G, which were used to calibrate trace element concentrations and monitor sensitivity drift. Raw effective image resolution along each line is ~2 times of the beam sizes. The complete maps were generated over a period of 2–3 h to keep instrument drift in sensitivity to the minimum. Iolite 4 software was used for processing the mapping data (Paton et al., 2011; Paul et al., 2012).

3.2. LA-MC-ICP-MS sulfur isotope analysis

The *in-situ* sulfur isotope analyses of pyrite were carried out with a Neptune Plus MC-ICP-MS (Thermo Fisher Scientific, Bremen, Germany) equipped with a GeoLas HD ArF-193 nm laser ablation system (Coherent, Göttingen, Germany) in the Wuhan Sample Solution Analytical Technology Co., Ltd, Hubei, China. In the laser ablation system, helium was used as a carrier gas and was mixed with argon (makeup gas). The single spot ablation mode was used. In order to minimize down hole fractionation (Fu et al., 2016), a large spot size (44 μm) with low pulse frequency (2 Hz) were selected to analyze about 100 laser pulses in a single analysis. At the same time, a new signal-smoothing device was equipped downstream from the sample cell to efficiently eliminate short-term signal variation, especially for the slow pulse frequency condition (Hu et al., 2015). The laser fluence was kept constant at ~5 J/cm^2. The Neptune plus was equipped with 9 Faraday cups fitted with 1011 Ω resistors. Isotopes ^{32}S, ^{33}S and ^{34}S were collected simultaneously in three Faraday cups using static mode. The newly-designed X skimmer and Jet sampler cones in Neptune Plus were used to improve signal sensitivity. Nitrogen (4 mL/min) was introduced into the gas flow to reduce the polyatomic interferences. All measurements were performed using a medium-resolution with a revolving power (as defined by a peak edge width from 5 to 95% of the full peak height) that was always greater than 5000. A standard-sample bracketing method (SSB) was employed to correct for instrumental mass fractionation. To avoid the matrix effect, a pyrite standard PPP-1 was chosen as a reference material for correcting the natural pyrite samples (Fu et al., 2016). In addition, the in-house reference material pyrrhotite SP-Po-01 ($\delta^{34}S_{V\text{-}CDT}$ = 1.4‰ ± 0.4‰) and pyrite SP-PY-01 ($\delta^{34}S_{V\text{-}CDT}$ = -2.0‰ ± 0.5‰) were analyzed repeatedly as quality checks. Detailed instrument operating conditions and analytical test methods can be found in Fu et al. (2016). Data reduction for the MC-ICP-MS analysis of S isotope ratios

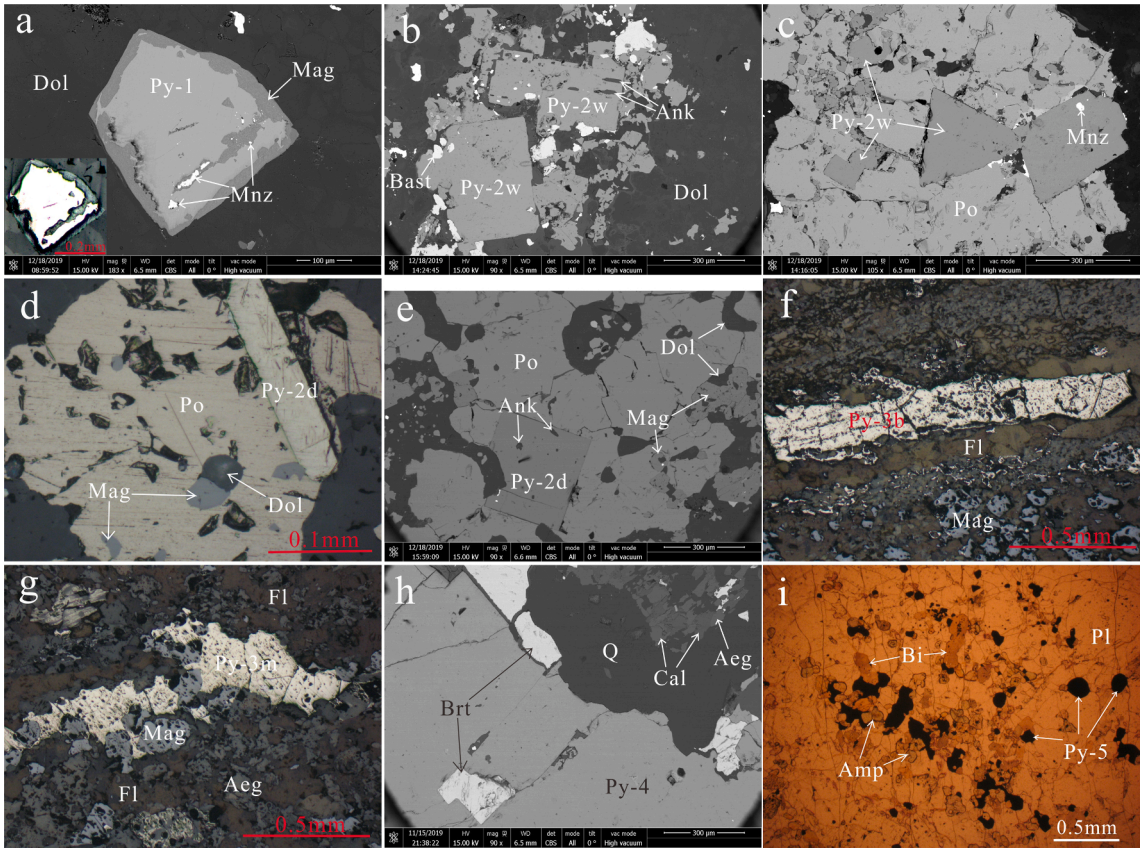

Fig. 4. Pyrite morphology and mineral association in different types of rocks and ores. **a:** Pyrite in ore-hosting dolomite was replaced by magnetite, and monazite was precipitated; **b-c:** Pyrite in dolomite of Western Open Pit is associated with pyrrhotite, magnetite, bastnäsite, ankerite and dolomite; **d-e:** Pyrite in dolomite of deep boreholes of Main and East Open Pits is symbiotic with pyrrhotite, magnetite, dolomite and ankerite; **f:** Pyrite in banded REEs-Nb-Fe ores; **g:** Subhedral pyrite in massive aegirine type ores; **h:** Coarse grained pyrite associated with barite, quartz and calcite in vein ores. **i:** Granular pyrite in skarn. Aeg: aegirine; Ank: ankerite; Amp: amphibole; Bast: bastnäsite; Bi: biotite; Brt: barite; Cal: calcite; Dol: dolomite; Mag: magnetite; Mnz: monazite; Pl: plagioclase; Po: pyrrhotite; Py: pyrite; Q: quartz.

was processed using the "Iso-Compass" software (Zhang et al., 2020).

4. Pyrite petrography

There are several types of sulfides in the Bayan Obo mining area, mainly pyrite, pyrrhotite, sphalerite and galena. However, only pyrite is the most widely distributed sulfide. According to the field occurrence, mineral paragenetic association and microstructure characteristics, pyrites collected from different types of rocks and ores in the Bayan Obo deposit are preliminarily divided into the following five categories in this contribution. The classification is only for the purpose of comparative study on the differences between all kinds of pyrites.

Py-1 occurs in the ore-hosting dolomite in the north of the Main Open Pit, which is disseminated and has euhedral granular morphology (Fig. 3a). The pyrite grains are usually replaced pseudomorphically by magnetite along the grain edge, and monazite can be seen locally with magnetite (Fig. 4a). The transformed body still retains the pentagonal dodecahedron form of pyrite, and the contact boundary with dolomite grains (no deformation and recrystallization) is straight and closely intergrown. Since the host rocks of Py-1 have not suffered from the late hydrothermal alteration, and the combination of magnetite and monazite corresponds to the weak iron and rare earth mineralization during the crystallization of carbonatite magma (Yang et al., 2019), the geochemical information of Py-1 can be used to indicate the characteristics of pre-carbonatite stage.

Py-2w, widely distributed in the ore-hosting dolomite in the West Open Pit, has euhedral granular texture (Fig. 3c), and is generally associated with pyrrhotite, bastnäsite, and dolomite (Fig. 4b-c). There are mineral inclusions in pyrite, such as ankerite, and monazite (Fig. 4b). Compared with the Main and East Open Pits, the West Open Pit suffered less late hydrothermal alteration, so pyrite in the West Open Pit is less likely to be modified. Py-2d is mainly distributed in the dolomite of deep boreholes in the periphery areas of the Main and East Open Pits. It has euhedral granular texture and is often associated with pyrrhotite, dolomite, apatite, bastnäsite, monazite and magnetite (Fig. 3b, 4d-e). There are inclusions in pyrite, such as ankerite, dolomite and bastnäsite. Both Py-2w and Py-2d are euhedral and associated with pyrrhotite, which is similar to the primary sulfide in typical carbonatite (Mitchell and Krouse, 1975; Farrell et al., 2010). They crystallize at the same time as carbonatite magma, so they are later than Py-1.

Py-3 was formed in the hydrothermal mineralization stage of the late carbonatite magma evolution (Liu et al., 2018a), and includes pyrite extending along the bands of the banded ores (Py-3b; Fig. 3d, 4f) and euhedral-subhedral granular pyrite in massive aegirine type ore (Py-3 m; Fig. 3e, 4 g). Both pyrites are generally associated with magnetite, aegirine, riebeckite and fluorite.

Py-4 is a typical mineral of the early Paleozoic vein ores, with large particle size (greater than1 cm) and euhedral crystal (Liu et al., 2018a). They are widely distributed in the upper part of Main and East ore bodies, and commonly associated with barite, quartz, aegirine and calcite (Fig. 3f, 4 h). They usually cut through all kinds of ores occurring as coarse-grained veins, and Liu et al. (2004) reported the Py-4 age of 439 ± 86 Ma by the Re-Os dating method.

Py-5 occurs in the eastern contact zone (Fig. 1), where skarnization took place between ore-hosting dolomite and granite, and formed in the late Paleozoic (~270 Ma; Fan et al., 2009; Ling et al., 2014). Pyrite is

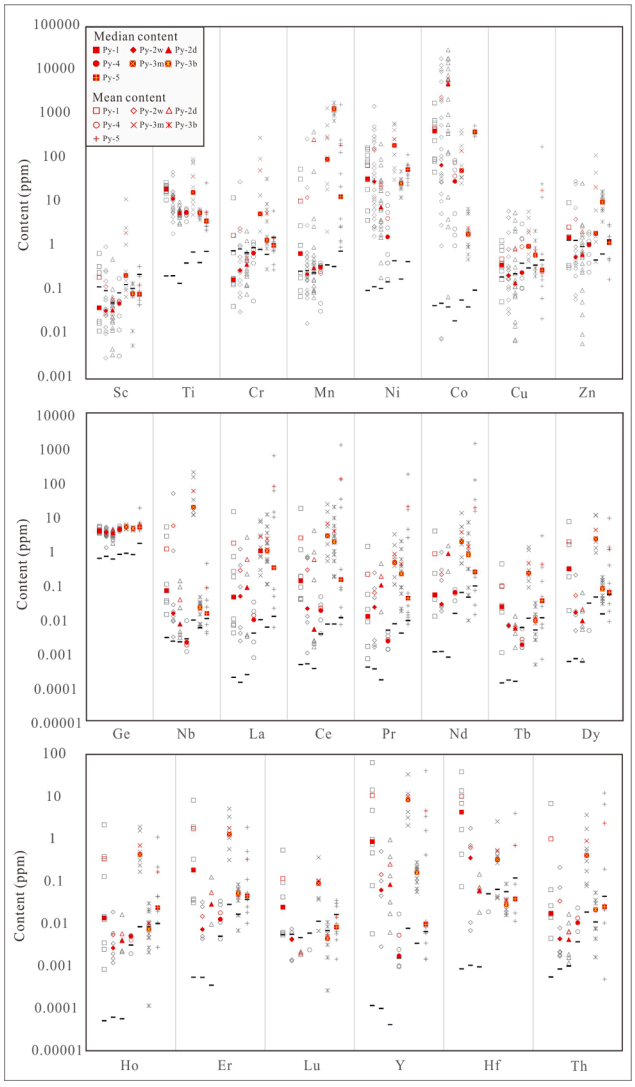

Fig. 5. Ranges and medians of LA-ICP-MS trace element contents of different pyrites, Bayan Obo. The black horizontal bar is the mean detection limit.

distributed in skarn as anhedral disseminated grains, and associated with biotite and amphibole (Fig. 3g, 4i).

5. Results

5.1. Spot and mapping analyses of trace elements of pyrite

The trace element contents of Py-1 (n = 11), Py-2w (n = 17), Py-2d (n = 18), Py-3b (n = 12), Py-3 m (n = 8), Py-4 (n = 8) and Py-5 (n = 12) were determined by LA-ICP-MS. Amongst 35 elements, V, Ga, Rb, Sr, In, Ba, Sm, Eu, Gd, Tm, Yb, and U were below the detection limits; whereas Sc, Ti, Cr, Mn, Co, Ni, Cu, Zn, Ge, Y, Nb, La, Ce, Pr, Nd, Tb, Dy, Ho, Er, Lu, Hf, and Th are in appreciable concentrations. All spot analytical results of pyrite from Bayan Obo deposit are given in Supplementary Table 2 and Fig. 5. The median values and median absolute deviations of trace element contents in pyrite are listed in Table 1. All pyrite types have similar Ge content (Table 1; Fig. 5) and are enriched in LREEs (Figs. 5, 6e). In general, pyrites have quite variable trace element contents spanning five orders of magnitude (Fig. 5). Scandium, Tb, Ho, and Lu contents are lower than ~1 ppm; Cu, Ge, Dy, Er, Hf and Th contents are lower that ~10 ppm; Ti, Cr, Zn, Nb, La, Ce, Pr, Nd and Y contents are lower that ~100 ppm; Ni contents are lower that ~1000 ppm; Mn contents are up to ~1800 ppm; and Co contents are up to ~30000 ppm.

In generally, Py-1 has relatively high contents of Ti (median of 20.5 ppm), Mn (0.7 ppm), Ni (35.1 ppm), Nb (0.1 ppm), Hf (4.3 ppm) and REEs. Py-2w and Py-2d have similar contents of Ti, Mn, Ni, Co, Cu, Ge, Nb and REEs, with undetectable Sc, Cr, Zn and Lu. It indicates that the deep dolomite of the Main-East Open Pits may have similar geochemical characteristics to those of the West Open Pit, and the alteration degree of the deep dolomite of the Main-East Open Pits is not as strong as that of the shallow one. Among all types of pyrites, Py-3 m has the highest Sc (0.2 ppm), Cr (5.6 ppm), Ni (202 ppm), Nb (17.5 ppm) and Y (8.4 ppm). Py-3b has the highest Mn (1400 ppm) and Zn (10.3 ppm), and the lowest Co (1.9 ppm). In addition, Py-3b and Py-3 m have the highest LREEs contents (La, Ce, Pr and Nd) among all types of pyrites. Compared with other types of pyrite, Py-4 is generally lower in the content of Ti, Ni, La, Ce, Nd, Ho, Er and Y, and the median contents of Sc, Cr, Mn, Cu, Zn, Nb, Pr, Tb, Dy and Lu are lower than the detection limit. Py-5 has relatively high contents of Mn (13.7 ppm), Co (406 ppm) and Ni (56.9 ppm), with low and variable contents of niobium and rare earth elements.

Py-1 has the highest ratios of Y/Ho (Fig. 6b) with the total rare earth content varies greatly (Fig. 6e), and has similar ranges of content ratios of La/Ho and La/Yb to Py-2w and Py-2d (Fig. 6d, f). Compared with Py-2w and Py-2d, the Ni content of Py-1 is relatively higher, so the Co/Ni ratio is smaller (Table 1; Fig. 6a, c). Py-2w and Py-2d have similar Co/Ni, Y/Ho, La/Ho and La/Yb and high rare earth contents (Fig. 6). Py-3b has the lowest Co/Ni ratio (Fig. 6a, c), and its Y/Ho, La/Ho and La/Yb are consistent with those of K-rich slate of Bilute Formation (Fig. 6b, d, f). Py-3 m has the highest Ni content and relatively low ratio of Co/Ni, and has similar La/Ho and La/Yb ratios to Py-1, Py-2w and Py-2d (Table 1; Fig. 6a, d, f). The Co/Ni ratio of Py-4 varies widely, and the Y/Ho ratio is the lowest (Fig. 6b). Compared with Py-3 m and Py-3b, the Y/Ho, La/Ho, La/Yb and total rare earth contents of Py-4 are lower (Fig. 6b, d-f). Compared with Py-2w and Py-2d, Py-5 has lower Co/Ni ratio and its rare earth content varies significantly, but the Y/Ho, La/Ho and La/Yb ratios of the three are similar (Fig. 6).

The trace element mapping (Fig. 7) showed that compared with magnetite rims and host mineral dolomite, Py-1 was enriched in Co by 2–3 orders of magnitude, but depleted in Ba, Sr, Ni and Cr. The REEs and Nb contents of Py-1 and magnetite is generally lower than those of dolomite, while the REEs distribution in Py-1 is extremely heterogeneous, and there may be micro-inclusions obviously enriched in LREEs. There was no trace element content change for Py-2 to Py-5 in the line analysis, so trace element mapping was not carried out for them.

5.2. In-situ sulfur isotope composition of pyrite

A total of 79 pyrite grains *in-situ* sulfur isotope compositions were determined (Table 2 and Fig. 8). Py-1 is the most enriched ^{34}S in all types of pyrites in Bayan Obo deposit, and its $\delta^{34}S$ ranges from +8.6‰ to +13.8‰ (avg = +12.1‰, n = 11). The $\delta^{34}S$ of Py-2w ranges from −1.0‰ to +3.0‰ (avg = +1.6‰, n = 16). The $\delta^{34}S$ of Py-2d is similar to that of Py-2w, ranging from −1.0‰ to +3.7‰ (avg = +1.6‰, n = 12). Py-3 m and Py-3b represent the sulfur isotopic composition of pyrite in the REEs-Fe ores of Bayan Obo deposit. The $\delta^{34}S$ of Py-3 m is similar to that of Py-2w and Py-2d, ranging from +0.2‰ to +2.4‰ (avg = +1.7‰, n = 7). The sulfur isotope values of Py-3b are significantly higher than those of pyrite in ore-hosting dolomite (Py-2w and Py-2d) and massive ore (Py-3 m), and are similar to those of pyrite in potassium-rich slate of Bilute Formation (Py-S, ranging from + 6.8‰ to +9.1‰ with an average of +8.1‰, Liu et al., 2018a), ranging from +5.7‰ to +7.7‰ (avg = +6.7‰, n = 7). Compared with other types of pyrites, Py-4 is enriched in ^{32}S and $\delta^{34}S$ is the lowest, ranging from −2.0‰ to +2.7 ‰ (avg = -0.6‰, n = 14). The $\delta^{34}S$ of Py-5 is +9.1‰ to +10.8‰ (avg = +9.6‰, n = 12), which falls into the range of global granite sulfur isotopes (Sasaki and Ishihara, 1979; Santosh and Masuda, 1991; Seal, 2006; Marini et al., 2011).

Table 1
The statistical results of LA-ICP-MS on pyrites in the Bayan Obo deposit.

Type	Item	Sc	Ti	Cr	Mn	Ni	Co	Cu	Zn	Ge	Nb	La	Ce	Pr	Nd	Tb	Dy	Ho	Er	Lu	Y	Hf	Th
Py-1	Median	bdl	20.5	bdl	0.70	35.1	426	0.38	1.63	3.46	0.06	0.04	0.12	0.01	0.05	0.02	0.28	0.01	0.19	0.02	0.87	4.32	0.02
	MAD	0.03	2.61	0.04	0.60	31.1	315	0.15	1.25	0.29	0.03	0.04	0.09	0.01	0.04	0.01	0.26	0.01	0.15	0.02	0.83	4.06	0.01
(n = 11)	Maximum	0.70	28.8	12.9	57.8	177	1844	1.37	10.0	4.79	4.62	12.9	16.1	1.25	3.50	0.38	6.62	2.18	8.24	0.55	63.8	38.7	6.92
	Minimum	bdl	11.6	bdl	bdl	3.97	49.8	bdl	bdl	3.01	0.01	bdl	0.03	bdl	0.01	bdl	0.02	bdl	0.03	bdl	0.01	0.08	bdl
Py-2w	Median	bdl	12.2	bdl	bdl	30.3	71.3	0.22	bdl	3.21	0.01	0.04	0.02	0.02	0.03	bdl	0.01	bdl	0.01	bdl	0.06	0.36	bdl
	MAD	0.02	4.13	0.21	0.15	27.4	70.7	0.11	0.23	0.35	0.01	0.04	0.02	0.02	0.01		0.01		0.01		0.04	0.35	0.01
(n = 17)	Maximum	1.00	50.0	29.7	283	1554	18,772	6.46	30.6	4.59	44.0	1.04	0.63	0.21	0.84	bdl	0.18	bdl	0.03	bdl	0.51	1.79	0.21
	Minimum	bdl	1.98	bdl	bdl	1.72	bdl	bdl	bdl	1.14	bdl	bdl	bdl	bdl	0.02	bdl	bdl	bdl	bdl	bdl	bdl	0.01	bdl
Py-2d	Median	bdl	5.92	bdl	0.33	7.96	4964	bdl	bdl	3.08	0.01	0.08	0.01	0.09	0.76	bdl	0.01	bdl	0.03	bdl	0.08	0.06	bdl
	MAD	0.02	0.71	0.22	0.23	6.33	4589	0.13	0.58	0.56	0.01	0.13	0.01	0.19	0.01		0.01		0.06		0.13	0.02	
(n = 18)	Maximum	0.52	10.3	2.27	407	217	29,872	5.92	27.6	17.8	0.12	2.30	3.60	0.39	1.29	bdl	0.05	bdl	0.13	bdl	0.96	0.15	bdl
	Minimum	bdl	3.26	bdl	bdl	0.20	0.07	bdl	bdl	1.53	bdl	bdl	bdl	0.02	0.23	bdl	bdl	bdl	0.01	bdl	0.01	0.02	bdl
Py-3 m	Median	0.22	17.1	5.59	96.9	202	53.8	1.03	2.02	4.65	17.5	0.92	2.54	0.42	1.74	0.21	2.07	0.43	1.29	0.09	8.44	0.33	0.41
	MAD	0.13	11.0	4.04	85.8	159	21.4	0.53	1.15	0.47	7.11	0.71	1.99	0.30	1.34	0.06	0.66	0.15	0.48	0.03	3.70	0.23	0.28
(n = 8)	Maximum	12.0	98.2	300	1409	633	442	6.28	119	5.43	184	7.06	21.3	2.81	11.7	1.18	10.2	1.95	5.19	0.37	33.7	2.61	3.71
	Minimum	bdl	5.35	0.88	2.19	33.1	27.6	0.47	bdl	3.92	10.3	0.18	0.46	0.10	0.39	0.08	0.81	0.17	0.32	bdl	2.10	bdl	0.08
Py-3b	Median	bdl	5.94	1.41	1362	27.6	1.93	0.64	10.3	4.15	0.02	0.93	1.70	0.20	0.72	0.01	0.07	bdl	0.05	bdl	0.17	bdl	0.02
	MAD	0.06	0.58	0.55	111	5.27	0.94	0.31	3.14	0.20	0.01	0.61	1.11	0.14	0.54	0.01	0.04	0.01	0.02		0.04	0.01	0.01
(n = 12)	Maximum	0.15	7.08	34.8	1869	51.4	7.26	2.28	18.0	4.46	0.04	10.6	17.8	1.76	6.28	0.03	0.16	0.03	0.08	bdl	0.28	0.09	0.05
	Minimum	bdl	4.14	bdl	731	13.2	0.51	bdl	3.71	3.66	0.01	0.10	0.16	0.02	bdl	bdl	0.03	bdl	bdl	bdl	0.06	bdl	bdl
Py-4	Median	bdl	6.03	bdl	bdl	1.68	30.7	bdl	bdl	3.89	bdl	0.01	0.02	bdl	0.06	bdl	bdl	bdl	0.01	bdl	bdl	bdl	0.01
	MAD	0.02	0.79	0.35	0.06	1.37	29.3	0.15	0.67	0.24		0.01	0.01		0.01				0.01				0.01
(n = 8)	Maximum	0.19	7.34	1.29	0.43	16.1	92.7	3.31	2.15	4.96	bdl	0.03	0.04	bdl	0.07	bdl	bdl	bdl	0.03	bdl	bdl	bdl	0.02
	Minimum	bdl	3.68	bdl	bdl	0.18	1.05	bdl	bdl	3.47	bdl	bdl	bdl	bdl	0.03	bdl	bdl	bdl	bdl	bdl	bdl	bdl	0.01
Py-5	Median	bdl	3.85	bdl	13.7	56.9	406	bdl	bdl	4.54	0.01	0.29	0.13	0.04	0.22	0.03	0.06	0.02	0.05	bdl	0.01	bdl	bdl
	MAD	0.02	1.18	0.39	12.6	15.4	24.4	0.20	0.71	0.30	0.01	0.29	0.13	0.03	0.21	0.03	0.04	0.02	0.03	0.01	0.01	0.02	0.02
(n = 12)	Maximum	0.36	28.3	6.47	1704	124	563	187	3.18	16.4	0.39	560	1151	160	1265	2.54	8.31	1.11	1.89	0.04	40.9	4.02	12.2
	Minimum	bdl	2.3	bdl	0.98	24.8	321	bdl	bdl	3.59	bdl	bdl	bdl	bdl	bdl	bdl	bdl	bdl	bdl	bdl	bdl	bdl	bdl

Notes: MAD = median absolute deviation. bdl = below detection limit.

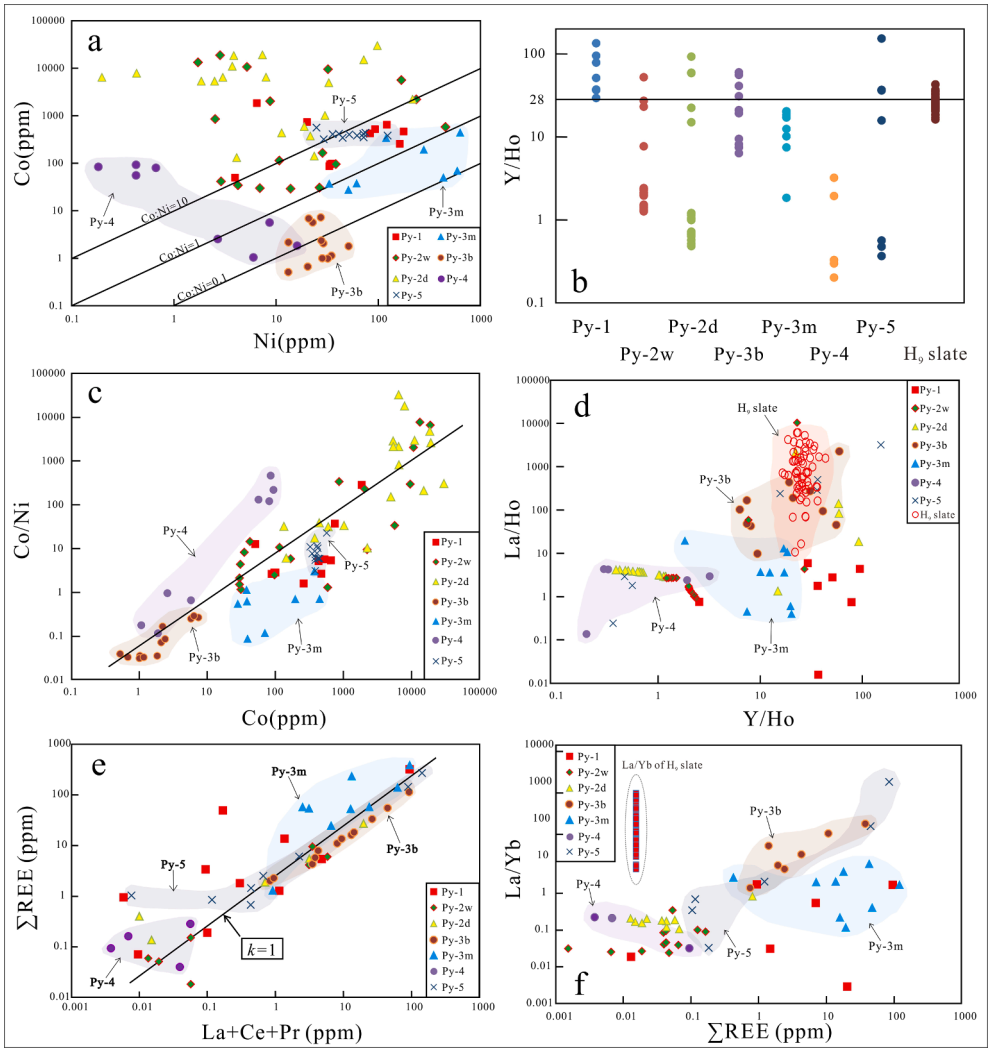

Fig. 6. Scatter diagrams of trace elements for different pyrites in Bayan Obo. (a) Co vs. Ni; (b) Y/Ho ratios; (c) Co/Ni vs. Co; (d) La/Ho vs. Y/Ho; (e) ∑REE vs. (La + Ce + Pr); (f) La/Yb vs. ∑REE. The chondrite values used for the normalization of rare earth elements are derived from Sun and McDonough. (1989). Trace element contents of H_9 K-rich slate of Bilute formation are derived from unpublished data.

6. Discussion

6.1. *The rare earth elements in Bayan Obo pyrite*

Typically, pyrite is depleted in REEs due to the large difference in ionic radius and charge between $REEs^{3+}$ (0.98–1.16 Å) and Fe^{2+} (0.76 Å; Shannon, 1976; Railsback, 2003; Jordens et al., 2013), making substitution difficult. Where seen, REEs may occur as micro-inclusions observable in Fig. 7. To evaluate the influence of REE micro-inclusions, using the correction method of Stepanov et al. (2020) to eliminate the influence of matrix composition on the pyrite trace elements content in black shale, we determined that mineral inclusions may have only contributed less than 0.1 ppm REEs in the Bayan Obo pyrite. Therefore, the REEs content of the Bayan Obo pyrite obtained in this study is little affected by mineral inclusions, which is consistent with the indications of the mineral concentration obtained by previous studies and the time-resolved spectra characteristics in this contribution. The accumulated *in-situ* trace element data shows that the REEs contents of dolomite (8–878 ppm), apatite (6230–18900 ppm), fluorite (540–8785 ppm), Na-amphibole (7–233 ppm) and aegirine (9–95 ppm), which may exist as mineral inclusions in pyrite, are much higher than those in pyrite, arguing against a mineral inclusion scenario (Liu et al., 2018a, 2018b; Hu et al., 2019; Chen et al., 2020). In addition, the time-resolved spectra show no REEs spikes caused by nanoparticles REEs-bearing minerals (Fig. 9). Moreover, it should be noted that the Bayan Obo pyrite crystallized in REE-rich environments (up to 25 wt% REE_2O_3 in typical ores). In this extremely REEs-enriched environment (ore-forming fluid with REEs of n wt.%; Gagnon et al., 2003; Tang et al., 2021), even if we give a very low distribution coefficient ($D_{Pyrite/Fluid}$ = 0.0001), the pyrite crystallized in this condition can sequester n ppm of REEs in their structure through lattice defects or adsorption (MacDonald et al., 2013; Borst et al., 2020). In different types of the Bayan Obo pyrite, the median content of REEs is lower and generally less than 10 ppm, very few samples can reach 100 ppm (Fig. 5). Recently, many studies have shown that there are certain contents of REEs in pyrite of gold-bearing quartz vein, and polymetallic sulfide ore of gold deposit, and pyrite in late Permian coals (10–340 ppm; Ustundag et al., 2007; Tang and Zhu, 2008; Mao et al., 2010; Zheng et al., 2010; Zhang et al., 2012; Jiang et al., 2016; Wang et al., 2017).

Above all, we believe that REEs mainly exist in the form of mineral inclusions in the pyrite, and it is important to emphasize that REEs also can exist in the structure of the Bayan Obo pyrite at several ppm or lower concentration.

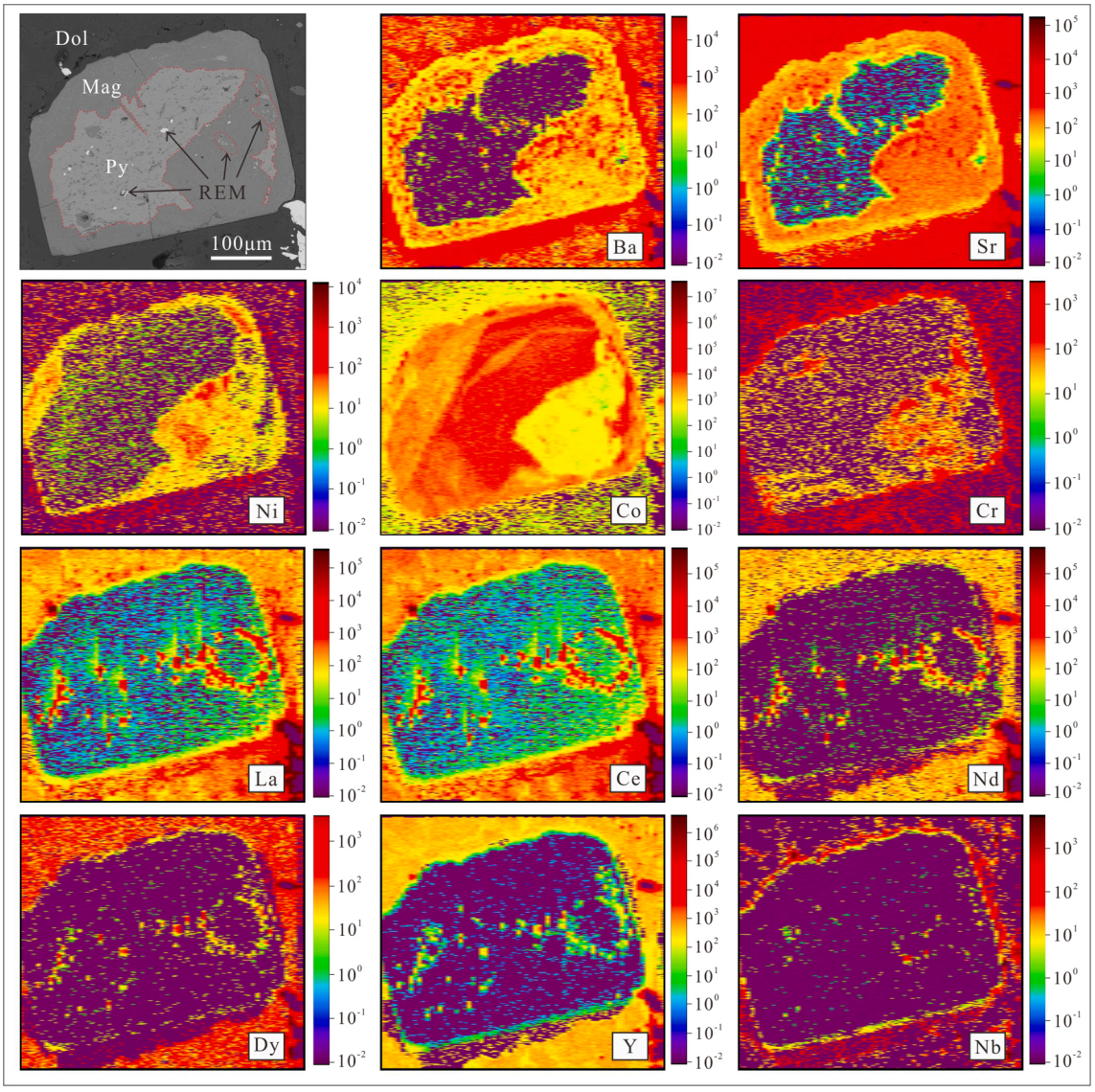

Fig. 7. LA-ICP-MS maps of elemental variation in core pyrite (Py-1) with rim magnetite. The upper left corner is BSE image of the pyrite, and the scales of concentration are in parts per million. Dol: Dolomite, Mag: magnetite, Py: Pyrite, REM: rare earth minerals.

6.2. Origin and source of ore-hosting dolomite

The origin of ore-hosting dolomite, hosting rare earth resources in Bayan Obo, has been controversial (igneous or sedimentary) for a long time (Wang et al., 1994; Le Bas et al., 1997; Yang et al., 2009, 2019). Despite of low amounts, primary pyrites (Py-1, Py-2w, and Py-2d) with obvious differences in texture and mineral assemblage in this contribution are found, providing new perspectives into the genesis of ore-hosting dolomite by *in-situ* trace element and sulfur isotope analyses of pyrite.

More previous estimates for the sulfur isotopic composition of the mantle suggests that the values of $\delta^{34}S$ is fairly constant and close to 0‰ based on the reference sulfur standard from the Canyon Diablo meteorite (Rye and Ohmoto, 1974; Ripley, 1999). However, a large number of mantle-originated materials have sulfur isotopic compositions deviating from the chondritic value in varying degrees ($\delta^{34}S$: −9 to +17‰ for mafic intrusions, Ohmoto, 1986; +2.0 to +20.7‰ for island arc rocks, Woodhead et al., 1987; +2.3 to +8.2‰ for sulfides in diamond, Chaussidon et al., 1987; −11 to +14‰ for sulfides in diamond, Eldridge et al., 1991), indicating that the sulfur isotopic compositions of the mantle are heterogeneous. Similarly, the sulfur isotopic values of carbonatites vary significantly (Fig. 8; −11 to +5‰, Mitchell and Krouse, 1975; −20 to +5‰, Deines, 1989; −24.6 to −0.8‰, Gomide et al., 2013; −15 to +15‰, Bolhar et al., 2020), and each carbonatite seems to have an independent range of sulfur isotopic composition (Grinenko et al., 1970; Mitchell and Krouse, 1975; Deines, 1989; Farrell et al., 2010). The distribution of sulfur isotope of pyrite in ore-hosting dolomite at Bayan Obo is similar (Fig. 8). The sulfur isotope of Py-1 ranges from +8.6‰ to +13.8‰ (mean of +12.1‰), which obviously deviates from the values of mantle and is different from the significantly variable $\delta^{34}S$ of sedimentary sources (Seal, 2006; Marini et al., 2011). The origin of ore-hosting dolomite in Bayan Obo has been suggested as igneous carbonatite (Campbell et al., 2014; Yang et al., 2019; Liu et al., 2020) or sedimentary carbonate metasomatized by carbonatite related fluid (Chao et al., 1997; Yang et al., 2009, 2017). Assuming that the ore-hosting dolomite and the high $\delta^{34}S$ of Py-1 are of sedimentary origin, then Py-2 formed by the metasomatism of carbonatite related fluid (low sulfur content, $\delta^{34}S$: 0‰) should have a significantly higher $\delta^{34}S$ than that of magma. However, this is not the case for the obtained the $\delta^{34}S$ of Py-2, so the high $\delta^{34}S$ of Py-1 is of magmatic origin, not sedimentary carbonate. Moreover, Py-1 has a highly Co/Ni ratio and is enriched in Ti, Ni, Nb, Hf and REEs (Fig. 5; 6a), with the content of trace elements

Table 2
Sulfur isotopic compositions of sulfides analyzed by LA-MC-ICP-MS in the Bayan Obo deposit.

Sample No.	Mineralogy	$^{34}S/^{32}S$	$\delta^{34}Sv\text{-}_{CDT}$ (‰)	Operation parameters
10BY10-3-1	Py-1	0.048924	13.5	44 μm, 2 Hz, 5 J/cm^2
10BY10-4-1	Py-1	0.048919	13.4	44 μm, 2 Hz, 5 J/cm^2
10BY10-4-2	Py-1	0.048866	12.3	44 μm, 2 Hz, 5 J/cm^2
10BY10-5-1	Py-1	0.048944	13.8	44 μm, 2 Hz, 5 J/cm^2
10BY10-5-2	Py-1	0.048905	13.0	44 μm, 2 Hz, 5 J/cm^2
10BY10-5-3	Py-1	0.048765	10.1	44 μm, 2 Hz, 5 J/cm^2
10BY10-5-4	Py-1	0.048928	13.5	44 μm, 2 Hz, 5 J/cm^2
10BY10-5-5	Py-1	0.048771	10.2	44 μm, 2 Hz, 5 J/cm^2
10BY10-5-6	Py-1	0.048920	13.2	44 μm, 2 Hz, 5 J/cm^2
10BY10-5-7	Py-1	0.048682	8.6	44 μm, 2 Hz, 5 J/cm^2
10BY10-5-8	Py-1	0.048864	12.0	44 μm, 2 Hz, 5 J/cm^2
17BY76-1	Py-2w	0.048400	2.5	44 μm, 2 Hz, 5 J/cm^2
17BY76-2	Py-2w	0.048411	2.7	44 μm, 2 Hz, 5 J/cm^2
17BY76-3	Py-2w	0.048386	2.2	44 μm, 2 Hz, 5 J/cm^2
19BY95-1	Py-2w	0.048431	3.0	44 μm, 2 Hz, 5 J/cm^2
19BY95-2	Py-2w	0.048404	2.4	44 μm, 2 Hz, 5 J/cm^2
19BY95-3	Py-2w	0.048394	2.1	44 μm, 2 Hz, 5 J/cm^2
19BY114-1	Py-2w	0.048336	0.7	44 μm, 2 Hz, 5 J/cm^2
19BY114-2	Py-2w	0.048360	1.2	44 μm, 2 Hz, 5 J/cm^2
19BY117-1	Py-2w	0.048438	2.9	44 μm, 2 Hz, 5 J/cm^2
19BY117-2	Py-2w	0.048372	1.5	44 μm, 2 Hz, 5 J/cm^2
19BY117-3	Py-2w	0.048421	2.4	44 μm, 2 Hz, 5 J/cm^2
19BY117-4	Py-2w	0.048399	2.0	44 μm, 2 Hz, 5 J/cm^2
19BY117-5	Py-2w	0.048431	2.7	44 μm, 2 Hz, 5 J/cm^2
19BY135-1	Py-2w	0.048350	−1.0	44 μm, 2 Hz, 5 J/cm^2
19BY135-2	Py-2w	0.048431	−0.7	44 μm, 2 Hz, 5 J/cm^2
19BY135-3	Py-2w	0.048362	−0.7	44 μm, 2 Hz, 5 J/cm^2
WK1505-134-1	Py-2d	0.048465	3.4	44 μm, 2 Hz, 5 J/cm^2
WK1505-134-2	Py-2d	0.048473	3.5	44 μm, 2 Hz, 5 J/cm^2
WK1505-137-1	Py-2d	0.048363	1.3	44 μm, 2 Hz, 5 J/cm^2
WK1505-137-2	Py-2d	0.048368	1.4	44 μm, 2 Hz, 5 J/cm^2
WK1505-137-3	Py-2d	0.048458	3.2	44 μm, 2 Hz, 5 J/cm^2
WK1505-146-1	Py-2d	0.048409	2.2	44 μm, 2 Hz, 5 J/cm^2
WK1505-146-2	Py-2d	0.048383	1.7	44 μm, 2 Hz, 5 J/cm^2
WK1505-146-3	Py-2d	0.048482	3.7	44 μm, 2 Hz, 5 J/cm^2
WK1505-64-1	Py-2d	0.048305	0.1	44 μm, 2 Hz, 5 J/cm^2
WK1505-64-2	Py-2d	0.048285	−0.3	44 μm, 2 Hz, 5 J/cm^2
WK1505-64-3	Py-2d	0.048310	0.2	44 μm, 2 Hz, 5 J/cm^2
WK1505-64-4	Py-2d	0.048252	−1.0	44 μm, 2 Hz, 5 J/cm^2
17BY19-1	Py-3m	0.048437	2.4	44 μm, 2 Hz, 5 J/cm^2
17BY19-2	Py-3m	0.048438	2.4	44 μm, 2 Hz, 5 J/cm^2
17BY19-3	Py-3m	0.048426	2.2	44 μm, 2 Hz, 5 J/cm^2
17BY77-1	Py-3m	0.048386	1.4	44 μm, 2 Hz, 5 J/cm^2
17BY77-2	Py-3m	0.048325	0.2	44 μm, 2 Hz, 5 J/cm^2
17BY77-3	Py-3m	0.048413	1.8	44 μm, 2 Hz, 5 J/cm^2
17BY77-4	Py-3m	0.048387	1.3	44 μm, 2 Hz, 5 J/cm^2
17BY166-1	Py-3b	0.048659	7.1	44 μm, 2 Hz, 5 J/cm^2
17BY166-2	Py-3b	0.048602	6.0	44 μm, 2 Hz, 5 J/cm^2
17BY166-3	Py-3b	0.048662	7.1	44 μm, 2 Hz, 5 J/cm^2
17BY166-4	Py-3b	0.048668	7.1	44 μm, 2 Hz, 5 J/cm^2
17BY166-5	Py-3b	0.048605	5.9	44 μm, 2 Hz, 5 J/cm^2
17BY166-6	Py-3b	0.048596	5.7	44 μm, 2 Hz, 5 J/cm^2
17BY166-7	Py-3b	0.048698	7.7	44 μm, 2 Hz, 5 J/cm^2
19BY13-1	Py-4	0.048267	−0.2	44 μm, 2 Hz, 5 J/cm^2
19BY13-2	Py-4	0.048284	−0.7	44 μm, 2 Hz, 5 J/cm^2
19BY13-3	Py-4	0.048283	1.0	44 μm, 2 Hz, 5 J/cm^2
19BY13-4	Py-4	0.048306	2.7	44 μm, 2 Hz, 5 J/cm^2
19BY13-5	Py-4	0.048283	1.2	44 μm, 2 Hz, 5 J/cm^2
19BY13-6	Py-4	0.048277	−0.8	44 μm, 2 Hz, 5 J/cm^2
19BY13-7	Py-4	0.048271	−0.9	44 μm, 2 Hz, 5 J/cm^2
19BY16-1	Py-4	0.048239	−1.7	44 μm, 2 Hz, 5 J/cm^2
19BY16-2	Py-4	0.048232	−1.8	44 μm, 2 Hz, 5 J/cm^2
19BY16-3	Py-4	0.048225	−2.0	44 μm, 2 Hz, 5 J/cm^2
19BY16-4	Py-4	0.048245	−1.5	44 μm, 2 Hz, 5 J/cm^2
19BY16-5	Py-4	0.048290	−0.6	44 μm, 2 Hz, 5 J/cm^2
19BY16-6	Py-4	0.048242	−1.6	44 μm, 2 Hz, 5 J/cm^2
19BY16-7	Py-4	0.048228	−1.8	44 μm, 2 Hz, 5 J/cm^2
19BY74A-1	Py-5	0.048808	10.8	44 μm, 2 Hz, 5 J/cm^2
19BY74A-2	Py-5	0.048737	9.3	44 μm, 2 Hz, 5 J/cm^2
19BY74A-3-1	Py-5	0.048747	9.5	44 μm, 2 Hz, 5 J/cm^2
19BY74A-3-2	Py-5	0.048761	9.9	44 μm, 2 Hz, 5 J/cm^2
19BY74A-4	Py-5	0.048745	9.6	44 μm, 2 Hz, 5 J/cm^2
19BY74A-6	Py-5	0.048739	9.4	44 μm, 2 Hz, 5 J/cm^2
19BY74B-2	Py-5	0.048769	9.6	

(*continued on next page*)

Table 2 (*continued*)

Sample No.	Mineralogy	$^{34}S/^{32}S$	$\delta^{34}S_{V\text{-}CDT}$ (‰)	Operation parameters
				44 μm, 2 Hz, 5 J/cm^2
19BY74B-3	Py-5	0.048753	9.3	44 μm, 2 Hz, 5 J/cm^2
19BY74B-4	Py-5	0.048734	9.1	44 μm, 2 Hz, 5 J/cm^2
19BY74B-5	Py-5	0.048762	9.8	44 μm, 2 Hz, 5 J/cm^2
19BY74B-6-1	Py-5	0.048742	9.5	44 μm, 2 Hz, 5 J/cm^2
19BY74B-6-2	Py-5	0.048762	9.6	44 μm, 2 Hz, 5 J/cm^2

varying over two orders of magnitude, which also indicates that it is unlikely to be of sedimentary origin (Bajwah et al., 1987; Clark et al., 2004; Monteiro et al., 2008; de Ronde et al., 2011; Large et al., 2014; Gregory et al., 2015, 2017). At the same time, it is also obviously different from the distribution characteristics of sedimentary pyrite in the form of euhedral granular or framboidal aggregate (Aragon and Miguens, 2001; Prol-Ledesma et al., 2010; Gregory et al., 2017). After crystallization, the edge of Py-1 is oxidized into magnetite and associated with monazite (Fig. 4a), while the host rocks of Py-1 have not been modified by the later hydrothermal process. It indicates that the formation of the "core-rim" phenomenon shown by pyrite and magnetite is synchronous with the crystallization of carbonate minerals, which is consistent with the weak precipitation of magnetite and monazite during the crystallization of carbonatite (Yang et al., 2019). Therefore, the geochemical characteristics of Py-1 can be used to indicate the geological characteristics of the pre-carbonatite stage. The high sulfur isotope values may be due to the contamination of oceanic crustal and sedimentary components, the alteration by seawater and the release of ^{32}S during mantle outgassing (Mitchell and Krouse, 1975; Deines, 1989; Zheng, 1990; Nikiforov et al., 2006; Marini et al., 2011; Hutchison et al., 2019). According to Rayleigh fractionation model, the removal of 99% initial sulfur with an extreme gas–melt fractionation can only give rise to an increase of 2.3‰ in the sulfur isotope composition of the residual phase (Sakai, 1957; Chaussidon et al., 1987), and thus cannot explain the values seen in Py1. In comparison, the oceanic crust altered by seawater-hydrothermal is enriched in ^{34}S, up to +10‰ (Albarède and Michard, 1986; Chaussidon et al., 1987), which is a suitable source of heavy sulfur isotope. Although the mixing of terrigenous materials in the process of magma migration can also cause a positive shift in sulfur isotope, whereas the viscosity of carbonatite magma is very low (Farrell et al., 2010), and can migrate quickly from the upper mantle to the shallow part of the crust and cool down, so the mixing is very weak, and it is difficult to cause such a large positive shift in sulfur isotope. Therefore, the contamination of the upper mantle by subducted oceanic crust may be the most reasonable explanation for the enrichment of heavy sulfur isotopes in Py-1 (Chaussidon et al., 1987; Woodhead et al., 1987; Eldridge et al., 1991; Ripley, 1999; Labidi et al., 2013; Bolhar et al., 2020), which can also explain the distribution of carbon ($\delta^{13}C$: −6.3 ~ 0.9‰) and oxygen isotopes ($\delta^{18}O$: 5.9 ~ 26.8‰) of ore-hosting dolomites between that of primary igneous carbonatites and marine limestones (Liu, 1986; Meng and Drew, 1992; Le Bas et al., 1997; Liu et al., 2020). A similar process also has been suggested to explain the $\delta^{15}N$ values from Zaire diamonds (Javoy et al., 1984), $\delta^{34}S$ values from

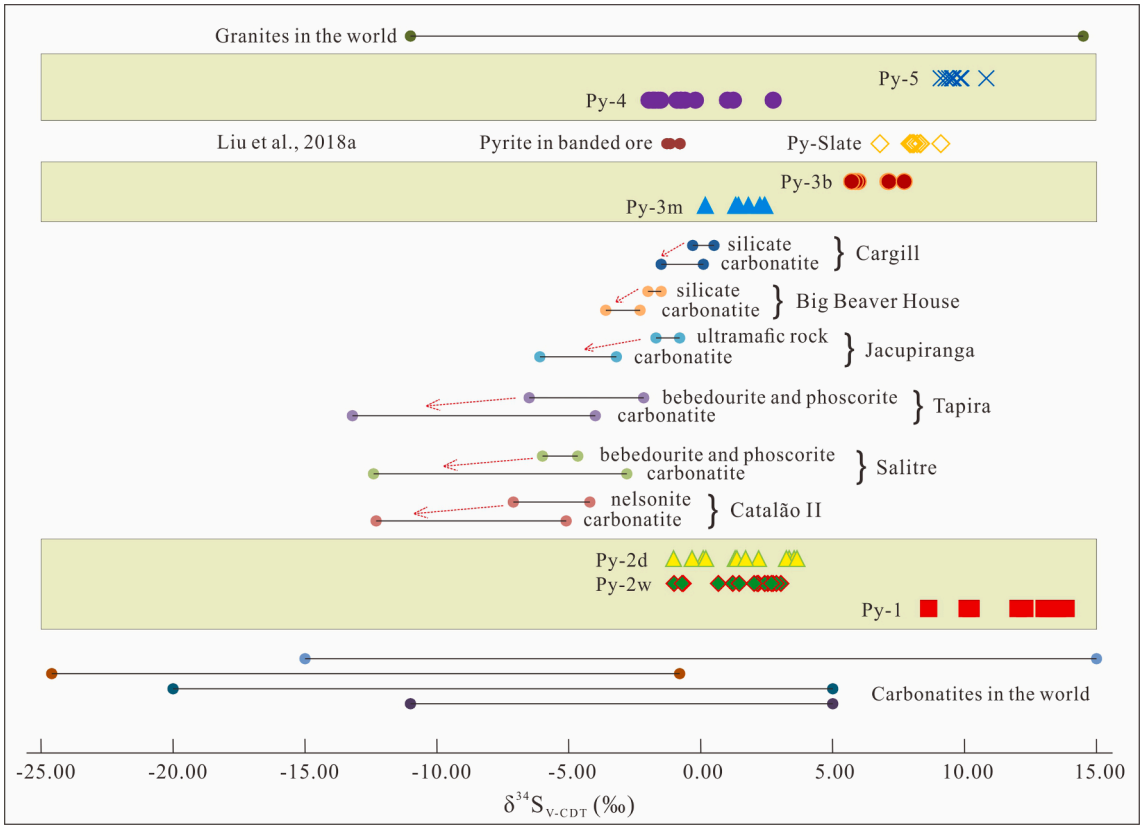

Fig. 8. The ranges of $\delta^{34}S$ of different types of pyrite analyzed by LA-MC-ICPMS in Bayan Obo. Data from this study are shown in light green background. Sulfur isotope values of pyrite (Py-Slate) in H_9 K-rich slate of Bilute formation and pyrite in banded ore are derived from Liu et al., (2018a). The statistical data of sulfur isotopes in carbonatites around the world are derived from Mitchell and Krouse, (1975), Deines, (1989), Gomide et al., (2013) and Bolhar et al., (2020). Sulphur isotopic values of carbonatites and associated rocks are derived from Mäkelä and Vartiainen, (1978), Farrell et al., (2010) and Gomide et al., (2013). The sulfur isotopic data of granites around the world came from Sasaki and Ishihara, (1979), Santosh and Masuda, (1991), Seal, (2006) and Marini et al., (2011). (For interpretation of the references to colour in this figure legend, the reader is referred to the web version of this article.)

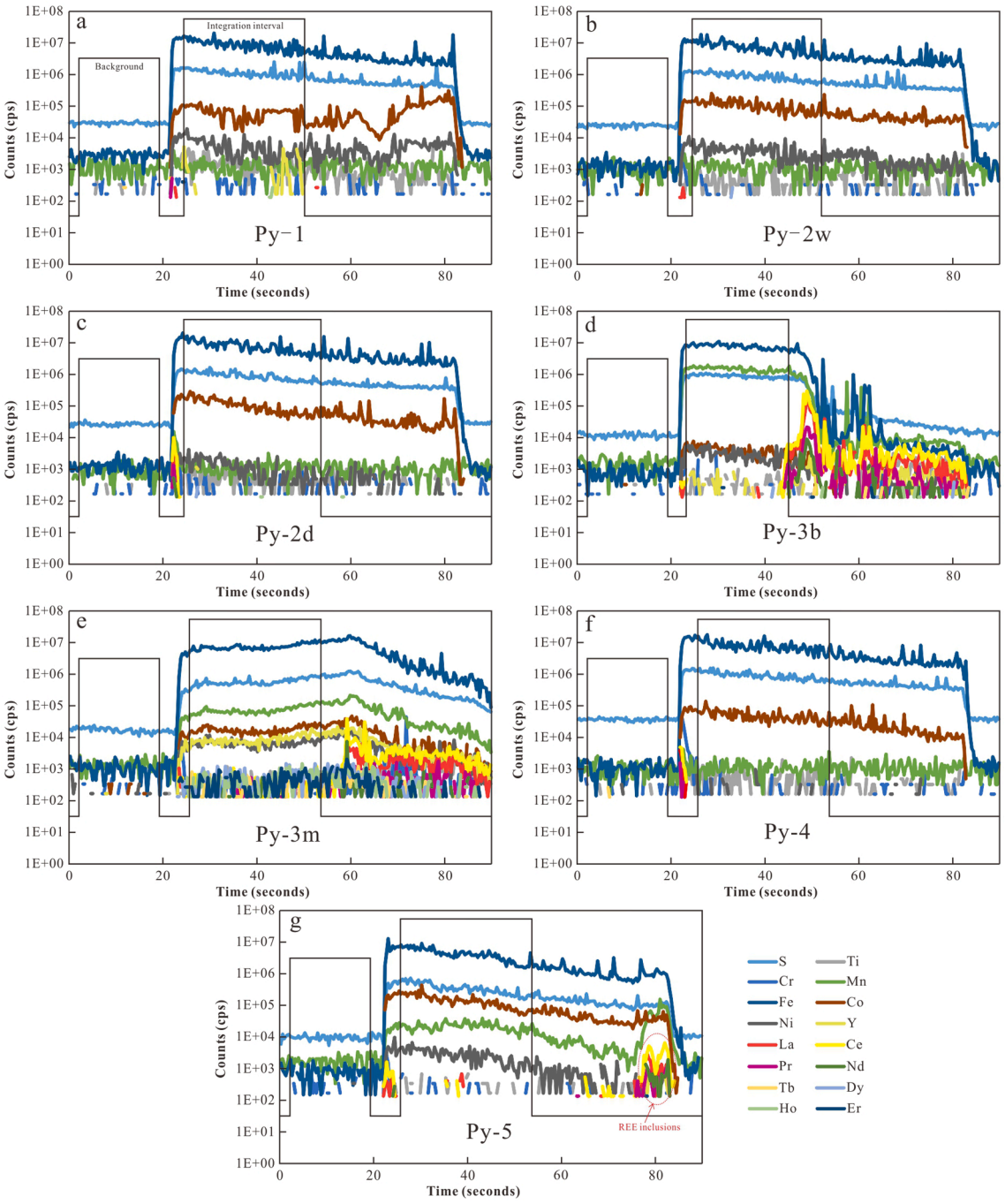

Fig. 9. Representative LA-ICP-MS time-resolved spectra for different kinds of pyrites in Bayan Obo.

Marianas island arc rocks (Woodhead et al., 1987), and light $\delta^{44/40}$Ca values for carbonatites (Amsellem et al., 2020) and the origin of Nolans Bore carbonatite (Anenburg et al., 2020).

Py-2w and Py-2d usually exist in the form of granular euhedral crystals and coexist with pyrrhotite (Fig. 4b-e). They are the main sulfur-containing minerals in ore-bearing dolomite, which is consistent with the occurrence of sulfur in typical carbonatite in the world (e.g. Schryburt Lake, Firesand River carbonatite; Mitchell and Krouse, 1975; Farrell et al., 2010). Considering the crystallization temperature (400–600 °C, Wang et al., 2010) and low oxygen fugacity [the pyrite-pyrrhotite buffer in Ohmoto (1972)] of ore-hosting dolomite, the sulfur isotope signature of Py-2 can reasonably represent the bulk sulfur isotope composition of the system (Ohmoto, 1972). The sulfur isotope values of Py-2w (average value: +1.6‰) and Py-2d (average value: +1.6‰) are significantly lower than those of Py-1. The sulfur isotope of Py-2 is of magmatic origin, which is consistent with the indications of the compositions of Pb isotope of dolomite, Sr, and O isotope of apatite in the ore-hosting dolomite (Yang et al., 2019; Chen et al., 2020). The extremely low viscosity leads to the rare addition of exogenous materials during the migration of carbonatite magma from the upper mantle to the crust (Farrell et al., 2010; Jones et al., 2013), so the sulfur isotope difference between Py-1 and Py-2 should be the result of the sulfur isotope fractionation within carbonatite system. Numerous studies shown that the alkaline silicate associated with carbonatite is usually enriched with heavy sulfur isotope (Fig. 8; Mäkelä and Vartiainen, 1978; Farrell et al., 2010; Gomide et al., 2013; Hutchison et al., 2019), which results in lower δ^{34}S value of carbonatite compared with associated alkaline silicate. In recent large-scale geological mapping, several contemporaneous

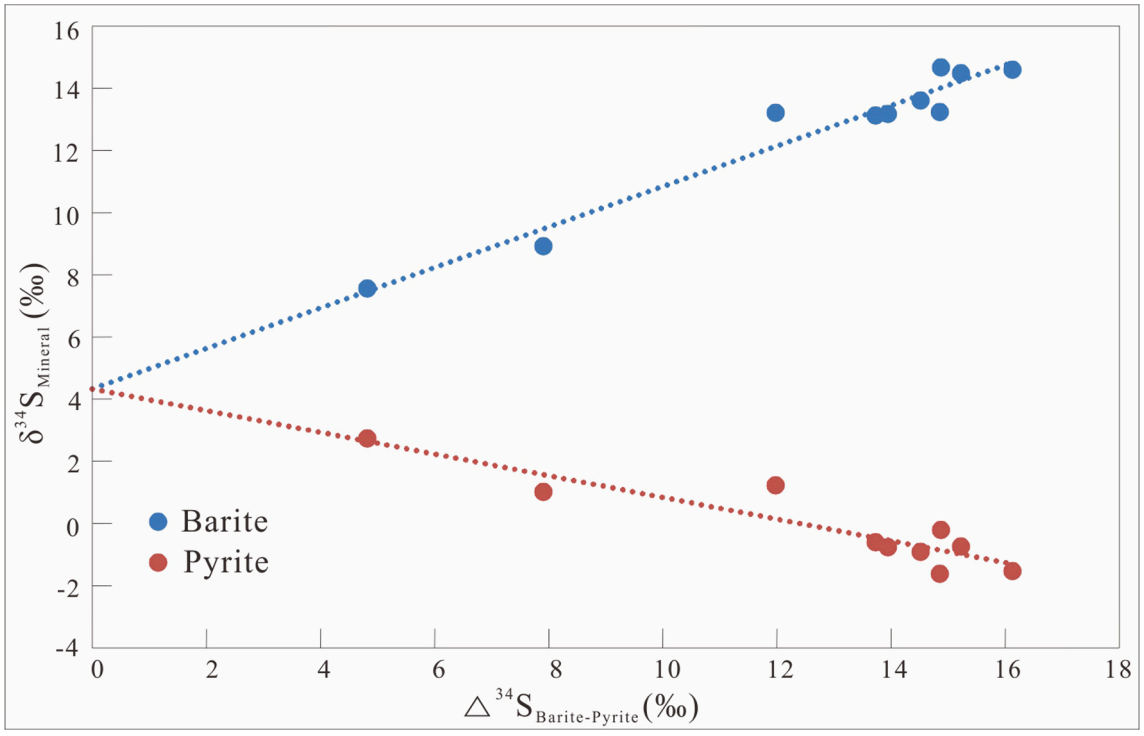

Fig. 10. The $\delta^{34}S_{mineral}$ versus $\triangle^{34}S_{Barite\text{-}Pyrite}$ diagram for sulfur isotope data from veined ores in Bayan Obo deposit. The data of barite sulfur isotope are derived from Liu et al., (2018a) and Lai et al., (2012).

alkaline rocks have been found around the Bayan Obo mining area (Wang et al., 2012), which indicates that the carbonatite differentiated from the alkaline silicate magma before intruding into the surrounding rock, and this differentiation may be an important factor for the decrease of Py-2 $\delta^{34}S$. In addition, from the early stage to the late stage of the carbonatite evolution, with the decrease of temperature and the increase oxygen fugacity, $\delta^{34}S$ also tends to decrease (Mitchell and Krouse, 1975; Mäkelä and Vartiainen, 1978; Deines, 1989; Drüppel et al., 2006; Farrell et al., 2010; Gomide et al., 2013; Hutchison et al., 2019). Therefore, the large sulfur isotope fractionation between Py-1 and Py-2 is probably the result of the combined effects of magmatic differentiation, cooling and increase of oxygen fugacity.

The Co/Ni ratios of Py-1, Py-2w and Py-2d are all greater than 1, indicating a magmatic-hydrothermal deposition environment (Fig. 6a, c; Hawley and Nichol, 1961; Bralia et al., 1979; Bajwah et al., 1987; Clark et al., 2004; Monteiro et al., 2008), which is consistent with the previous understanding of non-sedimentary origin. But the Co/Ni ratio of Py-1 is lower than that of Py-2. This is because Co tends to be enriched in pyrite and Ni in pyrrhotite (Neumann, 1950; Hawley and Nichol, 1961; Loftus-Hills et al., 1967) during the crystallization of Py-2, and Py-1 has a relatively high Ni content. These factors together lead to a low Co/Ni ratio of Py-1. In addition, Py-1 and Py-2 have similar La/Yb and La/Ho ratios, but the former has higher Y/Ho ratio. Y and Ho have similar geochemical properties, so they are called twin elements. The Y/Ho ratio of most igneous and clastic sedimentary rocks is about 28 (Bau and Dulski, 1995; Zhao and Jiang, 2007). However, the Y/Ho ratio of seawater and limestone is significantly higher than that of chondrite (Shabani et al., 1990; Bau et al., 1995; Minami et al., 1998). For example, the average Y/Ho ratio of the South Pacific seawater is 90–110 (Bau et al., 1995). The average Y/Ho ratios of Py-1 and Py-2 are 65.9 and 11.2 (Fig. 6b), respectively, which deviate from the chondrite values (ca. 28). Since a sedimentary origin of Py-1 has been basically ruled out in previous discussion, so the high Y/Ho ratio and $\delta^{34}S$ of Py-1 should be the result of the mixing of the subducted altered oceanic crust and upper mantle materials. Y may act as a Samarium-like light pseudo-lanthanide in carbonate-rich system, which is result in fractionation of Y and Ho and low Y/Ho ratio (Bau and Dulski, 1995). The Y/Ho ratio of Py-2 was significantly decreased (mean of 11.2) due to the extreme enrichment of carbonate in the carbonatite magmatic system, which was similar to the Y/Ho ratio of the ore-hosting dolomite (18.8–25, Liu et al., 2020).

Based on the above understanding, it is proposed that the ore-hosting dolomites are originated from the upper mantle carbonatitic magma which was contaminated by subducted oceanic crust ($\delta^{34}S$: ~ 12‰, Y/Ho: ~ 66), migrated upward to the shallow and underwent differentiation of mafic and silicate magma, then formed the carbonatite magma enriched light sulfur isotope ($\delta^{34}S$: ~ 1.6‰) with low Y/Ho ratio (Y/Ho: ~ 11) and intruded into the Bayan Obo group (Fig. 11a).

6.3. *Modification of mesoproterozoic materials by Paleozoic thermal events*

The Paleozoic thermal events can be divided into the early Paleozoic vein mineralization and the late Paleozoic granite intrusion. The former event forms a large number of coarse-grained REEs minerals and pyrite-bearing vein-type ores in the Main and East Open Pits. This kind of ores are common in the shallow part of the open pits and gradually diminish with depths. The latter event is characterized by large-scale granodioritic intrusion in the southeast of the mining area (Fig. 1). Skarnization occurs at the contact zone between the ore-hosting dolomite and the granitic intrusions. Meanwhile, small-scale iron mineralization exists locally.

In the early Paleozoic vein mineralization stage, pyrite and barite were closely associated, so the sulfur isotope value of pyrite was far less than that of fluid ($\delta^{34}S_{\sum S}$; Ohmoto, 1972). In order to obtain the sulfur isotopic composition of vein mineralized hydrothermal system, the isotopic composition of coexisting pyrite (Py-4) and barite pairs in the present study was plotted in the $\delta^{34}S$-$\triangle^{34}S_{barite\text{-}pyrite}$ diagram (Fig. 10; Pinckney and Rafter, 1972; Zheng, 2001), and the following two linear equations have been established:

$$\delta^{34}S_{barite} = 0.65\Delta^{34}S_{barite\text{-}pyrite} + 4.3 \quad (1)$$

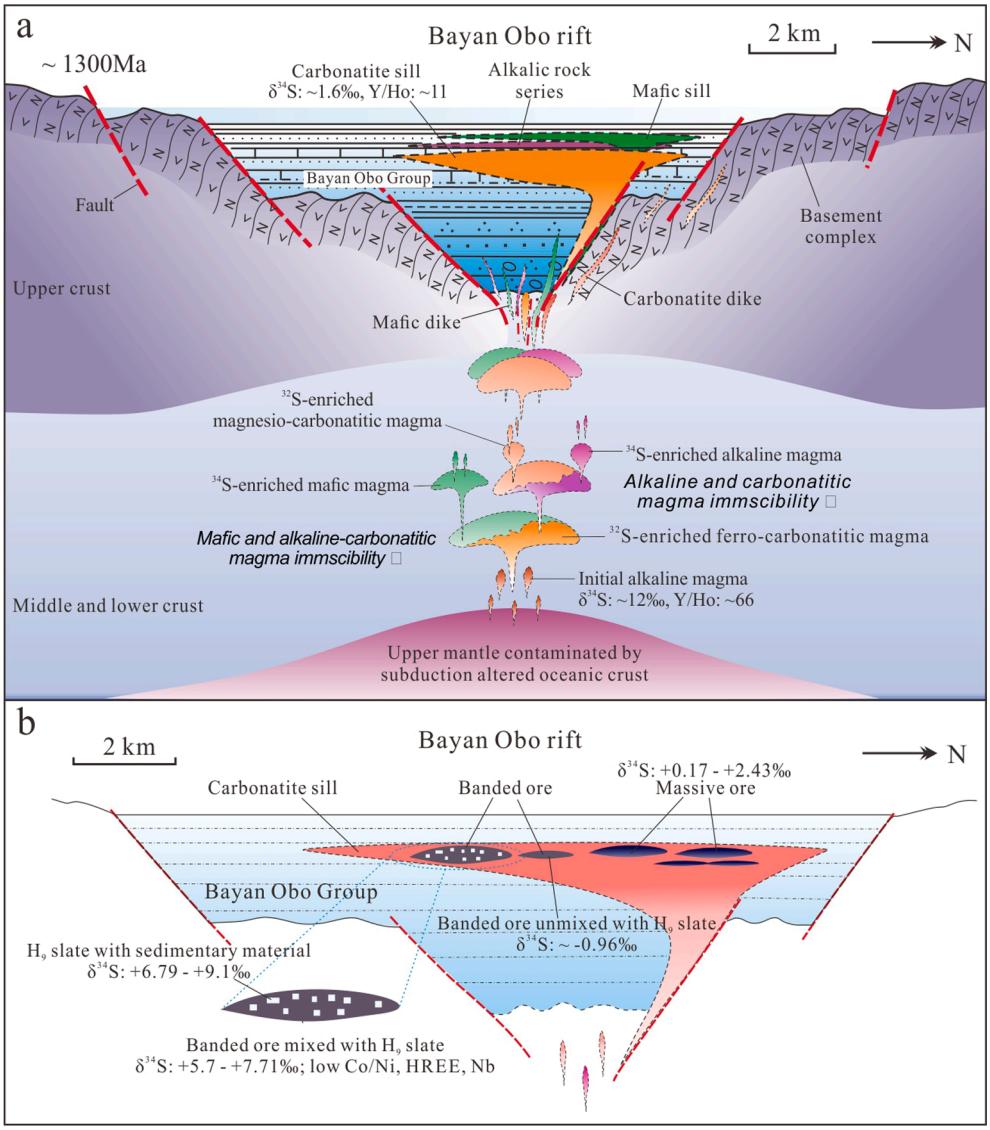

Fig. 11. **a:** The model for sulfur isotope evolution and genesis of carbonatite in the Mesoproterozoic Bayan Obo rift at 1300 Ma [revised from Yang et al., (2019)]. **b:** The banded ore was heterogeneously contaminated by K-rich H_9 slate during its formation, resulting in its sulfur isotope and trace element composition being obviously different from that of massive ore.

$$\delta^{34}S_{pyrite} = -0.35\Delta^{34}S_{barite\text{-}pyrite} + 4.3(2)$$

According to equations (1) and (2), the mole fractions of reduced sulfur and oxidized sulfur in the system are 0.65 and 0.35, respectively, and indicating that the sulfur isotope value of the system in the early Paleozoic vein mineralization stage is +4.3‰. The sulfur isotope value of +4.3‰ is significantly higher than that of Py-3 m (+0.2 to +2.4‰, with mean of +1.7‰), but lower than that of Py-3b (+5.7 to +7.7‰, with mean of +6.7‰) (Fig. 8). Except for Co, the content of trace elements in Py-4 is generally low, which is 2–3 orders of magnitude lower than that of Py-3 m and Py-3b (Fig. 5), especially Nb and REEs, and the Y/Ho ratio of Py-4 was significantly lower than that of Py-3 m and Py-3b (Fig. 6b). SEM-BSE images also show that Py-3b and Py-3 m are not modified by later thermal events. The large differences of trace elements and sulfur isotopes between pyrite in the main mineralization stage (Py-3 m and Py-3b) and pyrite in the vein mineralization stage (Py-4) shows that Py-3b and Py-3 m have not been affected by the fluid from the vein mineralization stage, which indicates that the reformation of early Paleozoic vein mineralization to Mesoproterozoic metallogenic materials is very weak, and it has little effect on the large-scale enrichment of rare earth resources in Bayan Obo.

The sulfur isotope value of Py-3 m is similar to that of Py-2 ($\delta^{34}S$: ~ 1.6‰), but Py-3b has significantly higher $\delta^{34}S$ than this value and deviates from the sulfur isotope range of carbonatites in this area. The contents of Sc, Ti, Cr, Ni, Co, Cu, Nb, Hf, Th and HREEs in Py-3b are significantly lower than those in Py-3 m, and the Co/Ni ratio ranges from 0.03 to 0.3 (Figs. 5, 6a). Sulfur isotope and trace element compositions of Py-3b indicates that there may be exogenous materials with relatively low HREEs content and sedimentary properties added in the formation of banded ore. Distinct from the differences between Py-3 m and Py-3b, Py-3b has similar Y/Ho, La/Ho, and La/Yb ratios with potassium-rich H_9 slate of Bilute Formation (REEs content of slate is unpublished data; Fig. 6b, d, f), and its sulfur isotope composition is close to that of pyrite in slate ($\delta^{34}S$: ~ 8.1‰; Fig. 8; Liu et al., 2018a). This indicates that the K-rich slate of the Bilute Formation was mixed in the banded mineralization stage (Fig. 11b), which resulted in the decrease of Co/Ni ratio, HREEs and Nb contents. However, Liu et al. (2018a) obtained that the sulfur isotope of pyrite in banded ore ranges from −1.3‰ to −0.8‰ (mean of −1.0‰; Fig. 8), which is quite different from that of Py-3b in this paper, indicating that the mixing of Bilute Formation slate is heterogeneous.

Compared with Py-3, Py-5 is enriched in Co and has a high Co/Ni ratio, but is depleted in Sc, Ti, Cr, Mn, Ni and Nb compared with Py-3 m,

while is depleted Mn and Zn compared with Py-3b (Figs. 5, 6a). In addition, the Y/Ho, La/Ho and La/Yb ratios of Py-5 vary widely, which are significantly different from those of Py-3 m and Py-3b (Fig. 6b, d, f). The contents of Cu and REEs in Py-5 vary by 3–5 orders of magnitude (Fig. 5), while these values of Py-3 vary in a small range. The median contents of Cu, La, Ce, Pr, Nd, Dy, Er and Y in Py-5 are lower than those in Py-3 m and Py-3b, and the contents of Tb, Ho and Lu in Py-5 are lower than those in Py-3 m, but higher than those in Py-3b. The whole rock trace element analysis of several granite samples in Bayan Obo by Ling et al. (2014) shows that the contents of La, Ce, Pr and Nd are generally high (10–150 ppm), while the contents of MREEs and HREEs are generally low (less than 5 ppm). This is similar to the trace elements of Py-5, but the contents of LREEs in a few samples are obviously beyond this range. This indicates that the material source of Py-5 is mainly derived from granite with a small amount of ore-bearing dolomite. Similar to trace elements, the sulfur isotopic value of Py-5 is also significantly different from those of Py-3 m and Py-3b, ranging from +9.1 to +10.8‰ (Fig. 8). The above differences in sulfur isotopes and trace elements indicate that Py-5 and Py-3 are of different origin, and Py-3 was not reformed by granite and its differentiated fluid, which also suggests that the granite emplacement event did not contribute to the enormous rare earth resources in Bayan Obo, and may only cause the low-grade re-enrichment of rare earth elements in the skarn between ore-hosting dolomite and granite.

7. Conclusions

Based on sulfur isotopes and trace elements of various generation/type pyrites in Bayan Obo deposit, the following progress has been made:

(1) Five types of pyrite were found from the intrusion of carbonatite magma, formed through the main metallogenic period to the Paleozoic thermal events, which caused obvious differences in trace elements and sulfur isotopic composition of pyrite;
(2) The ore-hosting dolomite is igneous carbonatite in origin and originated from the upper mantle contaminated with subducted oceanic crust ($\delta^{34}S$: ~ 12‰, Y/Ho: ~ 66), and underwent differentiation of silicate magma during migration upward to the shallow;
(3) The banded ore was heterogeneously contaminated by K-rich H_9 slate of Bilute Formation during its formation;
(4) The Paleozoic thermal events, including vein mineralization and granite intrusions, had limited contribution to the reformation of Mesoproterozoic metallogenic materials and the enrichment of large amounts of rare earth elements, may only cause the dissolution and re-enrichment of earlier metallogenic elements.

CRediT authorship contribution statement

Hai-Dong She: Investigation, Conceptualization, Methodology, Formal analysis, Writing – original draft. **Hong-Rui Fan:** Resources, Investigation, Conceptualization, Supervision, Writing – review & editing. **Kui-Feng Yang:** Resources, Investigation. **Xuan Liu:** Writing – review & editing. **Xing-Hui Li:** Writing – review & editing. **Zhi-Hui Dai:** Methodology, Formal analysis.

Declaration of Competing Interest

The authors declare that they have no known competing financial interests or personal relationships that could have appeared to influence the work reported in this paper.

Acknowledgments

We sincerely thank Er-Dou Li, Qiang Li, Zhang Liu, Hai-Long Jin and Zhen-Jiang Wang of Baotou Rare Earth Research Institute for their helps during the field works, and Ms. Xue Zhang of State Key Laboratory of Ore Deposit Geochemistry for her technical support in trace element analysis. We are grateful to Edit Frances Westall and three anonymous reviewers for their constructive feedback that helped to improve an earlier manuscript, and Matthew Steele-MacInnis for valuable suggestions. This work is funded by the National Natural Science Foundation of China (41930430, 91962103), the Key Research Program of the Institute of Geology and Geophysics, CAS (IGGCAS-201901), and the Opening Project of the State Key Laboratory of Baiyunobo Rare Earth Resource Researches and Comprehensive Utilization (2021H2280).

Appendix A. Supplementary material

Supplementary data to this article can be found online at https://doi.org/10.1016/j.precamres.2022.106801.

References

Abraitis, P.K., Pattrick, R.A.D., Vaughan, D.J., 2004. Variations in the compositional, textural and electrical properties of natural pyrite: a review. Int. J. Miner. Process. 74 (1-4), 41–59.
Agangi, A., Hofmann, A., Przybylowicz, W., 2014. Trace element zoning of sulfides and quartz at Sheba and Fairview gold mines: Clues to Mesoarchean mineralization in the Barberton Greenstone Belt, South Africa. Ore Geol. Rev. 56, 94–114.
Agangi, A., Hofmann, A., Wohlgemuth-Ueberwasser, C.C., 2013. Pyrite zoning as a record of mineralization in the Ventersdorp contact reef, Witwatersrand Basin, South Africa. Econ. Geol. 108 (6), 1243–1272.
Albarède, F., Michard, A., 1986. Transfer of continental Mg, S, O and U to the mantle through hydrothermal alteration of the oceanic-crust. Chem. Geol. 57 (1-2), 1–15.
Amsellem, E., Moynier, F., Betrand, H., Bouyon, A., Mata, J., Tappe, S., Day, J.M.D., 2020. Calcium isotopic evidence for the mantle sources of carbonatites. Sci. Adv. 6, eaba3269.
Anenburg, M., Mavrogenes, J.A., Bennett, V.C., 2020. The fluorapatite P-REE-Th vein deposit at Nolans Bore: genesis by carbonatite metasomatism. J. Petrol. 61, egaa003.
Aragon, G., Miguens, F., 2001. Microscopic analysis of pyrite in the sediments of two Brazilian mangrove ecosystems. Geo-Mar. Lett. 21 (3), 157–161.
Bai, G., Yuan, Z.X., Wu, C.Y., Zhang, Z.Q., Zheng, L.X., 1996. Demonstration on the Geological Features and Genesis of the Bayan Obo Ore Deposit. Geological Publishing House, Beijing in Chinese.
Bajwah, Z.U., Seccombe, P.K., Offler, R., 1987. Trace element distribution, Co/Ni ratios and genesis of the big cadia iron-copper deposit, new south wales, Australia. Miner. Deposita 22, 292–300.
Bau, M., Dulski, P., 1995. Comparative study of yttrium and rare-earth element behaviours in fluorine-rich hydrothermal fluids. Contrib. Mineral. Petrol. 119 (2-3), 213–223.
Bau, M., Dulski, P., Moller, P., 1995. Yttrium and Holmium in South-Pacific seawater-vertical-distribution and possible fractionation mechanisms. Chemie Der Erde-Geochem. 55, 1–16.
Belousov, I., Large, R.R., Meffre, S., Danyushevsky, L.V., Steadman, J., Beardsmore, T., 2016. Pyrite compositions from VHMS and orogenic Au deposits in the Yilgarn Craton, Western Australia: implications for gold and copper exploration. Ore Geol. Rev. 79, 474–499.
Bolhar, R., Whitehouse, M.J., Milani, L., Magalhães, N., Golding, S.D., Bybee, G., LeBras, L., Bekker, A., 2020. Atmospheric S and lithospheric Pb in sulphides from the 2.06 Ga Phalaborwa phoscorite-carbonatite Complex, South Africa. Earth Planet. Sci. Lett. 530, 115939.
Borst, A.M., Smith, M.P., Finch, A.A., Estrade, G., Villanova-de-Benavent, C., Nason, P., Marquis, E., Horsburgh, N.J., Goodenough, K.M., Xu, C., Kynicky, J., Geraki, K., 2020. Adsorption of rare earth elements in regolith-hosted clay deposits. Nat. Commun. 11, 1–15.
Bralia, A., Sabatini, G., Troja, F., 1979. A revaluation of the Co/Ni ratio in pyrite as geochemical tool in ore genesis problems. Miner. Deposita 14, 353–374.
Brill, B.A., 1989. Trace-element contents and partitioning of elements in ore minerals from the CSA Cu-Pb-Zn Deposit Australia and implications for ore genesis. Can. Mineral. 27, 263–274.
Campbell, L.S., Compston, W., Sircombe, K.N., Wilkinson, C.C., 2014. Zircon from the East Orebody of the Bayan Obo Fe-Nb-REE deposit, China, and SHRIMP ages for carbonatite-related magmatism and REE mineralization events. Contrib. Mineral. Petrol. 168, 1041.
Cao, R.L., Zhu, S.H., Wang, J.W., 1994. Material source and genesis of Bayan Obo iron rare earth deposit. Sci. China (Series B) 24, 1298–1307 in Chinese.
Chandra, A.P., Gerson, A.R., 2010. The mechanisms of pyrite oxidation and leaching: a fundamental perspective. Surf. Sci. Rep. 65 (9), 293–315.
Chao, E.C.T., Back, J.M., Minkin, J.A., Tatsumoto, M., Wang, J.W., Conrad, J.E., MaKee, E.H., Hou, Z.L., Meng, Q.R., Huang, S.G., 1997. The sedimentary carbonate-hosted giant Bayan Obo REE-Fe-Nb ore deposit of Inner Mongolia, China: a cornerstone example for giant polymetallic ore deposits of hydrothermal origin. US Geology Survey Bulletin 2143, 1–65.

Chao, E.C.T., Tatsumoto, M., Minkin, J.A., Back, J.M., Mckee, E.H., Ren, Y.C., Li, G.M., 1991. Muitiple lines of evidence for establishing the mineral paragenetic sequence of the Bayan Obo rare earth ore deposit of Inner Mongolia. China. Contr. Geol. Miner. Resour. Res. 6, 1–17 in Chinese with English abstract.
Chaussidon, M., Albarede, F., Sheppard, S.M.F., 1987. Sulfur Isotope Heterogeneity in the Mantle from Ion Microprobe Measurements of Sulfide Inclusions in Diamonds. Nature 330, 242–244.
Chen, W., Liu, H.-Y., Lu, J., Jiang, S.-Y., Simonetti, A., Xu, C., Zhang, W., 2020. The formation of the ore-bearing dolomite marble from the giant Bayan Obo REE-Nb-Fe deposit, Inner Mongolia: insights from micron-scale geochemical data. Mineral. Deposita 55 (1), 131–146.
Clark, C., Grguric, B., Mumm, A.S., 2004. Genetic implications of pyrite chemistry from the Palaeoproterozoic Olary Domain and overlying Neoproterozoic Adelaidean sequences, northeastern South Australia. Ore Geol. Rev. 25 (3-4), 237–257.
Craig, J.R., Vokes, F.M., Solberg, T.N., 1998. Pyrite: physical and chemical textures. Mineral. Deposita 34 (1), 82–101.
Craig, J.R., Vokes, F.M., 1993. The metamorphism of pyrite and pyritic ores: an overview. Mineral. Mag. 57 (386), 3–18.
Danyushevsky, L., Robinson, P., Gilbert, S., Norman, M., Large, R., McGoldrick, P., Shelley, M., 2011. Routine quantitative multi-element analysis of sulphide minerals by laser ablation ICP-MS: Standard development and consideration of matrix effects. Geochem. Explor. Environ. Anal. 11 (1), 51–60.
de Ronde, C.E.J., Massoth, G.J., Butterfield, D.A., Christenson, B.W., Ishibashi, J., Ditchburn, R.G., Hannington, M.D., Brathwaite, R.L., Lupton, J.E., Kamenetsky, V.S., Graham, I.J., Zellmer, G.F., Dziak, R.P., Embley, R.W., Dekov, V.M., Munnik, F., Lahr, J., Evans, L.J., Takai, K., 2011. Submarine hydrothermal activity and gold-rich mineralization at Brothers Volcano, Kermadec Arc, New Zealand. Mineral. Deposita 46 (5-6), 541–584.
Deditius, A.P., Utsunomiya, S., Reich, M., Kesler, S.E., Ewing, R.C., Hough, R., Walshe, J., 2011. Trace metal nanoparticles in pyrite. Ore Geol. Rev. 42 (1), 32–46.
Deines, P., 1989. Stable isotope variations in carbonatites. In: Bell, K. (Ed.), Carbonatites: Genesis and Evolution. Unwin Hyman, London, pp. 301–359.
Drew, L.J., Meng, Q.R., Sun, W.J., 1990. The Bayan Obo iron-rare earth-niobium deposits, Inner Mongolia, China. Lithos 26, 43–65.
Drüppel, K., Wagner, T., Boyce, A.J., 2006. Evolution of sulfide mineralization in ferrocarbonatite, Swartbooisdrif, Northwestern Namibia: constraints from mineral compositions and sulfur isotopes. Can. Mineral. 44, 877–894.
Eldridge, C.S., Compston, W., Williams, I.S., Harris, J.W., Bristow, J.W., 1991. Isotope evidence for the involvement of recycled sediments in diamond formation. Nature 353, 649–653.
Fan, H.R., Hu, F.F., Yang, K.F., Pirajno, F., Liu, X., Wang, K.Y., 2014. Integrated U-Pb and Sm-Nd geochronology for a REE-rich carbonatite dyke at the giant Bayan Obo REE deposit, Northern China. Ore Geol. Rev. 63, 510–519.
Fan, H.R., Hu, F.F., Yang, K.F., Wang, K.Y., Liu, Y.S., 2009. Geochronology framework of late Paleozoic dioritic-granitic plutons in the Bayan Obo area, Inner Mongolia, and tectonic significance. Acta Petrol. Sin. 25, 2933–2938 in Chinese with English abstract.
Fan, H.R., Yang, K.F., Hu, F.F., Liu, S., Wang, K.Y., 2016. The giant Bayan Obo REE-Nb-Fe deposit, China: controversy and ore genesis. Geosci. Front. 7, 335–344.
Fan, H.R., Yang, K.F., Hu, F.F., Wang, K.Y., Zhai, M.G., 2010. Zircon geochronology of basement rocks from the Bayan Obo area, Inner Mongolia, and tectonic implications. Acta Petrol. Sin. 26, 1342–1350 in Chinese with English abstract.
Farrell, S., Bell, K., Clark, I., 2010. Sulfur isotopes in carbonatites and associated silicate rocks from the Superior Province, Canada. Mineral. Petrol. 98, 209–226.
Feng, K., Fan, H.R., Groves, D.I., Yang, K.F., Hu, F.F., Liu, X., Cai, Y.C., 2020. Geochronological and sulfur isotopic evidence for the genesis of the post-magmatic, deeply sourced, and anomalously gold-rich Daliuhang orogenic deposit, Jiaodong, China. Mineral. Deposita 55, 293–308.
Fu, J.L., Hu, Z.C., Zhang, W., Yang, L., Liu, Y.S., Li, M., Zong, K.Q., Gao, S., Hu, S.H., 2016. In situ, sulfur isotopes ($\delta^{34}S$ and $\delta^{33}S$) analyses in sulfides and elemental sulfur using high sensitivity cones combined with the addition of nitrogen by Laser Ablation MC-ICP-MS. Anal. Chim. Acta 911, 14–26.
Gomide, C.S., Brod, J.A., Junqueira-Brod, T.C., Buhn, B.M., Santos, R.V., Barbosa, E.S.R., Cordeiro, P.F.O., Palmieri, M., Grasso, C.B., Torres, M.G., 2013. Sulfur isotopes from Brazilian alkaline carbonatite complexes. Chem. Geol. 341, 38–49.
Gagnon, J.E., Samson, I.M., Fryer, B.J., Williams-Jones, A.E., 2003. Compositional heterogeneity in fluorite and the genesis of fluorite deposits: insights from LA-ICP-MS analysis. Can. Mineral. 41, 365–382.
Gregory, D.D., Cracknell, M.J., Large, R.R., McGoldrick, P., Kuhn, S., Maslennikov, V.V., Baker, M.J., Fox, N., Belousov, I., Figueroa, M.C., Steadman, J.A., Fabris, A.J., Lyons, T.W., 2019. Distinguishing ore deposit type and barren sedimentary pyrite using laser ablation-inductively coupled plasma-mass spectrometry trace element data and statistical analysis of large data sets. Econ. Geol. 114, 771–786.
Gregory, D.D., Large, R.R., Halpin, J.A., Baturina, E.L., Lyons, T.W., Wu, S., Danyushevsky, L., Sack, P.J., Chappaz, A., Maslennikov, V.V., Bull, S.W., 2015. Trace element content of sedimentary pyrite in black shales. Econ. Geol. 110, 1389–1410.
Gregory, D.D., Lyons, T.W., Large, R.R., Jiang, G.Q., Stepanov, A.S., Diamond, C.W., Figueroa, M.C., Olin, P., 2017. Whole rock and discrete pyrite geochemistry as complementary tracers of ancient ocean chemistry: an example from the Neoproterozoic Doushantuo formation, China. Geochim. Cosmochim. Acta 216, 201–220.
Grinenko, L.N., Kononova, V.A., Grinenko, V.A., 1970. Isotope composition of sulfide S in carbonatites. Geochem. Int. 7, 45–53.
Hao, Z.G., Wang, X.B., Li, Z., Xiao, G.W., Zhang, T.R., 2002. Bayan Obo carbonatite REE-Nb-Fe deposit: a rare example of Neoproterozoic lithogeny and metallogeny of a damaged volcanic edifice. Acta Geol. Sin. 76, 525–540 in Chinese with English abstract.
Hawley, J.E., Nichol, I., 1961. Trace elements in pyrite, pyrrhotite and chalcopyrite of different ores. Econ. Geol. 56, 467–487.
Hodkiewicz, P.F., Groves, D.I., Davidson, G.J., Weinberg, R.F., Hagemann, S.G., 2009. Influence of structural setting on sulphur isotopes in Archean orogenic gold deposits, Eastern Goldfields Province, Yilgarn, Western Australia. Mineral. Deposita 44, 129–150.
Hoefs, J., 2015. Stable Isotope Geochemistry, seventh ed. Springer International Publishing, Switzerland. doi: 10.1007/978-3-319-19716-6.
Hu, F.F., Fan, H.R., Liu, S., Yang, K.F., Chen, F., 2009. Sm-Nd and Rb-Sr isotopic dating of veined REE mineralization for the Bayan Obo REE-Nb-Fe deposit, northern China. Resour. Geol. 59, 407–414.
Hu, H.L., Fan, H.R., Liu, X., Cai, Y.C., Yang, K.F., Ma, W.D., 2020. Two-stage gold deposition in response to H_2S loss from a single fluid in the Sizhuang deposit (Jiaodong, China). Ore Geol. Rev. 120, 103450.
Hu, L., Li, Y.K., Wu, Z.J., Bai, Y., Wang, A.J., 2019. Two metasomatic events recorded in apatite from the ore-hosting dolomite marble and implications for genesis of the giant Bayan Obo REE deposit, Inner Mongolia, Northern China. J. Asian Earth Sci. 172, 56–65.
Hu, Z.C., Zhang, W., Liu, Y.S., Gao, S., Li, M., Zong, K.Q., Chen, H.H., Hu, S.H., 2015. "Wave" signal-smoothing and mercury-removing device for laser ablation quadrupole and multiple collector ICPMS analysis: application to lead isotope analysis. Anal. Chem. 87, 1152–1157.
Huston, D.L., Sie, S.H., Suter, G.F., Cooke, D.R., Both, R.A., 1995. Trace elements in sulfide minerals from eastern Australian volcanic-hosted massive sulfide deposits; Part 1, Proton microprobe analyses of pyrite, chalcopyrite, and sphalerite, and Part 2, Selenium levels in pyrite; comparison with Delta ^{34}S values and implications for the source of sulfur in volcanogenic hydrothermal systems. Econ. Geol. 90, 1167–1196.
Hutchison, W., Babiel, R.J., Finch, A.A., Marks, M.A.W., Markl, G., Boyce, A.J., Stueken, E.E., Friis, H., Borst, A.M., Horsburgh, N.J., 2019. Sulphur isotopes of alkaline magmas unlock long-term records of crustal recycling on Earth. Nat. Commun. 10, 4208.
IGCAS, 1988. Geochemistry of Bayan Obo deposit. Science Press, Beijing (in Chinese).
Javoy, M., Pineau, F., Demaiffe, D., 1984. Nitrogen and carbon isotopic composition in the diamonds of Mbuji-Mayi (Zaire). Earth Planet. Sci. Lett. 68, 399–412.
Jiang, Y.F., Qian, H.D., Zhou, G.Q., 2016. Mineralogy and geochemistry of different morphological pyrite in Late Permian coals. South China. Arabian J. Geosci. 9, 590.
Jin, L.Y., Qin, K.Z., Li, G.M., Li, Z.Z., Song, G.X., Meng, Z.J., 2015. Trace element distribution in sulfides from the Chalukou porphyry Mo-vein-type Zn-Pb system, northern Great Xing' an Range, China: Implications for metal source and ore exploration. Acta Petrol. Sin. 31, 2417–2434.
Jones, A.P., Genge, M., Carmody, L., 2013. Carbonate melts and carbonatites. Rev. Mineral. Geochem. 75, 289–322.
Jordens, A., Cheng, Y.P., Waters, K.E., 2013. A review of the beneficiation of rare earth element bearing minerals. Miner. Eng. 41, 97–114.
Keith, M., Haase, K.M., Klemd, R., Krumm, S., Strauss, H., 2016. Systematic variations of trace element and sulfur isotope compositions in pyrite with stratigraphic depth in the Skouriotissa volcanic-hosted massive sulfide deposit, Troodos ophiolite. Cyprus. Chem. Geol. 423, 7–18.
Labidi, J., Cartigny, P., Moreira, M., 2013. Non-chondritic sulphur isotope composition of the terrestrial mantle. Nature 501, 208–211.
Lai, X.D., Yang, X.Y., 2013. Geochemical characteristics of the Bayan Obo giant REE-Nb-Fe deposit: constraints on its genesis. J. South Am. Earth Sci. 41, 99–112.
Lai, X.D., Yang, X.Y., Liu, Y.L., Yan, Z.Q., 2016. Genesis of the Bayan Obo Fe-REE-Nb deposit: evidences from Pb-Pb age and microanalysis of the H8 Formation in Inner Mongolia, North China Craton. J. Asian Earth Sci. 120, 87–99.
Large, R.R., Halpin, J.A., Danyushevsky, L.V., Maslennikov, V.V., Bull, S.W., Long, J.A., Gregory, D.D., Lounejeva, E., Lyons, T.W., Sack, P.J., McGoldrick, P.J., Calver, C.R., 2014. Trace element content of sedimentary pyrite as a new proxy for deep-time ocean-atmosphere evolution. Earth Planet. Sci. Lett. 389, 209–220.
Large, R.R., Maslennikov, V.V., Robert, F., Danyushevsky, L.V., Chang, Z., 2007. Multistage sedimentary and metamorphic origin of pyrite and gold in the giant Sukhoi Log deposit, Lena gold province, Russia. Econ. Geol. 102, 1233–1267.
Le Bas, M.J., Spiro, B., Yang, X.M., 1997. Oxygen, carbon and strontium isotope study of the carbonatitic dolomite host of the Bayan Obo Fe-Nb-REE deposit, Inner Mongolia, N China. Mineral. Mag. 61, 531–541.
Li, J.Y., 2006. Permian geodynamic setting of Northeast China and adjacent regions: closure of the Paleo-Asian Ocean and subduction of the Paleo-Pacific Plate. J. Asian Earth Sci. 26, 207–224.
Li, X.C., Yang, K.F., Spandler, C., Fan, H.R., Zhou, M.F., Hao, J.L., Yang, Y.H., 2021a. The effect of fluid-aided modification on the Sm-Nd and Th-Pb geochronology of monazite and bastnäsite: Implication for resolving complex isotopic age data in REE ore systems. Geochim. Cosmochim. Acta 300, 1–24.
Li, X.C., Fan, H.R., Zeng, X., Yang, K.F., Yang, Z.F., Wang, Q.W., Li, H.T., 2021b. Identification of ~1.3 Ga hydrothermal zircon from the giant Bayan Obo REE deposit (China): implication for dating geologically-complicated REE ore system. Ore Geol. Rev. 138, 104405.
Li, X.H., Fan, H.R., Yang, K.F., Hollings, P., Liu, X., Hu, F.F., Cai, Y.C., 2018. Pyrite textures and compositions from the Zhuangzi Au deposit, southeastern North China Craton: implication for ore-forming processes. Contrib. Mineral. Petrol. 173, 73.
Ling, M.X., Zhang, H., Li, H., Liu, Y.L., Liu, J., Li, L.Q., Li, C.Y., Yang, X.Y., Sun, W.D., 2014. The Permian-Triassic granitoids in Bayan Obo, North China Craton: a geochemical and geochronological study. Lithos 190–191, 430–439.

Liu, S., Fan, H.R., Groves, D.I., Yang, K.F., Yang, Z.F., Wang, Q.W., 2020. Multiphase carbonatite-related magmatic and metasomatic processes in the genesis of the ore-hosting dolomite in the giant Bayan Obo REE-Nb-Fe deposit. Lithos 354–355, 105359.
Liu, S., Fan, H.R., Yang, K.F., Hu, F.F., Rusk, B., Liu, X., Li, X.C., Yang, Z.F., Wang, Q.W., Wang, K.Y., 2018a. Fenitization in the giant Bayan Obo REE-Nb-Fe deposit: implication for REE mineralization. Ore Geol. Rev. 94, 290–309.
Liu, S., Fan, H.R., Yang, K.F., Hu, F.F., Wang, K.Y., Chen, F.K., Yang, Y.H., Yang, Z.F., Wang, Q.W., 2018b. Mesoproterozoic and Paleozoic hydrothermal metasomatism in the giant Bayan Obo REE-Nb-Fe deposit: constrains from trace elements and Sr-Nd isotope of fluorite and preliminary thermodynamic calculation. Precambrian Res. 311, 228–246.
Liu, T.G., 1986. A discussion on the genesis of dolomite in Bayan Obo, Inner Mongolia with emphasis on the composition of oxygen and carbon isotopes. Geol. Rev. 32, 150–154 in Chinese with English abstract.
Liu, Y.L., Yang, G., Chen, J.F., Du, A.D., Xie, Z., 2004. Re-Os dating of pyrite from Giant Bayan Obo REE-Nb-Fe deposit. Chin. Sci. Bull. 49, 2627–2631.
Liu, Y.S., Hu, Z.C., Gao, S., Günther, D., Xu, J., Gao, C.G., Chen, H.H., 2008. In situ analysis of major and trace elements of anhydrous minerals by LA-ICP-MS without applying an internal standard. Chem. Geol. 257, 34–43.
Loftus-Hills, G., Solomon, M., 1967. Cobalt, nickel and selenium in sulphides as indicators of ore genesis. Mineral. Deposita 2, 228–242.
MacDonald, J.M., Wheeler, J., Harley, S.L., Mariani, E., Goodenough, K.M., Crowley, Q., Tatham, D., 2013. Lattice distortion in a zircon population and its effects on trace element mobility and U-Th-Pb isotope systematics: examples from the Lewisian Gneiss Complex, northwest Scotland. Contrib. Mineral. Petrol. 166, 21–41.
Mäkelä, M., Vartiainen, H., 1978. A study of S isotopes in the Sokli multi-stage carbonatite (Finland). Chem. Geol. 21, 257–265.
Mao, G.Z., Hua, R.M., Gao, J.F., Zhao, K.D., Long, G.M., Lu, H.J., Yao, J.M., 2010. Rare earth element and trace element features of gold-bearing pyrite in the Jinshan gold deposit, Jiangxi Province. Acta Geol. Sin. 84, 614–623.
Marini, L., Moretti, R., Accornero, M., 2011. Sulfur isotopes in magmatic-hydrothermal systems, melts, and magmas. Rev. Mineral. Geochem. 73, 423–492.
Maslennikov, V.V., Maslennikova, S.P., Large, R.R., Danyushevsky, L.V., 2009. Study of trace element zonation in vent chimneys from the silurian yaman-Kasy volcanic-hosted massive sulfide deposit (Southern Urals, Russia) using Laser Ablation-Inductively Coupled Plasma Mass Spectrometry (LA-ICPMS). Econ. Geol. 104, 1111–1141.
Meng, Q.R., 1982. The genesis of the host rock dolomite of Bayan Obo iron ore deposits and the analysis of its sedimentary environment. Geol. Rev. 28, 481–489 in Chinese with English abstract.
Meng, Q.R., Drew, L.J., 1992. Study on oxygen and carbon isotopes and the implication for genesis of Bayan Obo ore bearing H8 dolomite. Contr. Geol. Miner. Resour. Res. 7, 46–54 in Chinese with English abstract.
Meng, Y.M., Hu, R.Z., Huang, X.W., Gao, J.F., Sasseville, C., 2019. The origin of the carbonate-hosted Huize Zn-Pb-Ag deposit, Yunnan province, SW China: constraints from the trace element and sulfur isotopic compositions of pyrite. Mineral. Petrol. 113, 369–391.
Minami, M., Masuda, A., Takahashi, K., Adachi, M., Shimizu, H., 1998. Y-Ho fractionation and lanthanide tetrad effect observed in cherts. Geochem. J. 32, 405–419.
Mitchell, R.H., Krouse, H.R., 1975. Sulphur isotope geochemistry of carbonatites. Geochim. Cosmochim. Acta 39, 1505–1513.
Monteiro, L.V.S., Xavier, R.P., Hitzman, M.W., Juliani, C., de Souza, C.R., Carvalho, E.D., 2008. Mineral chemistry of ore and hydrothermal alteration at the Sossego iron oxide-copper-gold deposit, Carajas Mineral Province, Brazil. Ore Geol. Rev. 34, 317–336.
Mukherjee, I., Large, R.R., 2020. Co-evolution of trace elements and life in Precambrian oceans: the pyrite edition. Geology 48, 1018–1022.
Neumann, H., 1950. Pseudomorphs of pyrrhotite after pyrite in the Ballachulish slates. Mineral. Mag. 29, 234–238.
Nielsen, H., 1979. Sulfur isotopes. In: Jager, E., Hunziker, J. (Eds.), Lectures in isotope geology. Springer, Berlin, pp. 283–312.
Nikiforov, A.V., Bolonim, A.V., Pokrovsky, B.G., Sugorakova, A.M., Chugaev, A.V., Lykhin, D.A., 2006. Isotope geochemistry (O, C, S, Sr) and Rb/Sr age of carbonatites in Central Tuva. Geol. Ore Deposits 48, 256–276.
Ohmoto, H., 1972. Systematics of sulfur and carbon isotopes in hydrothermal ore deposits. Econ. Geol. 67, 551–578.
Ohmoto, H., 1986. Stable isotope geochemistry of ore deposits in Stable Isotopes in High Temperature Geological Processes. Rev. Mineral. Geochem. 16, 491–559. https://doi.org/10.1515/9781501508936-019.
Ohmoto, H., Goldhaber, M.B., 1997. Sulfur and carbon isotopes. In: Barnes, H.L. (Ed.), Geochemistry of hydrothermal ore deposits, 3rd ed. Wiley Interscience, New York, pp. 435–486.
Ohmoto, H., Rye, R.O., 1979. Isotopes of sulfur and carbon. Geochemistry of hydrothermal ore deposits, second ed. Holt Rinehart and Winston, New York.
Paton, C., Hellstrom, J., Paul, B., Woodhead, J., Hergt, J., 2011. Iolite: freeware for the visualization and processing of mass spectrometric data. J. Anal. Atom. Spectrom. 26, 2508–2518.
Paul, B., Paton, C., Norris, A., Woodhead, J., Hellstrom, J., Hergt, J., Greig, A., 2012. Cell Space: a module for creating spatially registered laser ablation images within the Iolite freeware environment. J. Anal. At. Spectrom. 27, 700–706.
Pinckney, D.M., Rafter, T.A., 1972. Fractionation of sulphur isotopes during ore deposition in the Upper Mississippi Valley zinc-lead district. Econ. Geol. 67, 315–328.
Price, B.J., 1972. Minor Elements in Pyrites from the Smithers Map Area, British Columbia and Exploration Applications of Minor Element Studies. University of British Columbia. Available from <https://open.library.ubc.ca/collections/ubctheses/831/items/1.0053102>.
Prol-Ledesma, R.M., Canet, C., Villanueva-Estrada, R.E., Ortega-Osorio, A., 2010. Morphology of pyrite in particulate matter from shallow submarine hydrothermal vents. Am. Mineral. 95, 1500–1507.
Qin, C.J., Qiu, Y.Z., Zhou, G.F., Wang, Z.G., Zhang, T.R., Xiao, G.W., 2007. Fluid inclusion study of carbonatite dykes/veins and ore-hosted dolostone at the Bayan Obo ore deposit. Acta Petrol. Sin. 23, 161–168 in Chinese with English abstract.
Railsback, L.B., 2003. An earth scientist's periodic table of the elements and their ions. Geology 31, 737–740.
Raymond, O.L., 1996. Pyrite composition and ore genesis in the Prince Lyell copper deposit, Mt Lyell mineral field, western Tasmania, Australia. Ore Geol. Rev. 10, 231–250.
Reich, M., Kesler, S.E., Utsunomiya, S., Palenik, C.S., Chryssoulis, S.L., Ewing, R.C., 2005. Solubility of gold in arsenian pyrite. Geochim. Cosmochim. Acta 69, 2781–2796.
Ripley, E.M., 1999. Systematics of S and O isotopes in mafic igneous rocks and related Cu-Ni-PGE mineralization. In: Keays RR, Lesher CM, Lightfoot PC, Farrow CEG (Eds.), Dynamic Processes in Magmatic Ore Deposits and Their Application to Mineral Exploration. GAC Short Course Notes 13, pp. 133–158.
Rye, R.O., Ohmoto, H., 1974. Sulfur and carbon isotopes and ore genesis: a review. Econ. Geol. 69, 826–842.
Sakai, H., 1957. Fractionation of sulphur isotopes in nature. Geochim. Cosmochim. Acta 12, 150–169.
Santosh, M., Masuda, H., 1991. Reconnaissance oxygen and sulfur isotopic mapping of Pan-African alkali granites and syenites in the southern Indian Shield. Geochem. J. 25, 173–185.
Sasaki, A., Ishihara, S., 1979. Sulfur isotopic composition of the magnetite-series and ilmenite-series granitoids in Japan. Contrib. Mineral. Petrol. 68, 107–115.
Seal, R.R., 2006. Sulfur isotope geochemistry of sulfide minerals. Reviews in Mineral. Geochem. 61, 633–677.
Shabani, M.B., Akagi, T., Shimizu, H., Masuda, A., 1990. Determination of trace lanthanides and yttrium in seawater by Inductively Coupled Plasma Mass-Spectrometry after preconcentration with solvent-extraction and back-extraction. Anal. Chem. 62, 2709–2714.
Shannon, R.D., 1976. Revised effective ionic radii and systematic studies of inter-atomic distance in halides and chalcogenides. Acta Crystallogr. Sect. A 32, 751–757.
She, H.D., Fan, H.R., Yang, K.F., Li, X.C., Wang, Q.W., Zhang, L.F., Liu, S., Li, X.H., Dai, Z. H., 2021. In situ trace elements of magnetite in the Bayan Obo REE-Nb-Fe deposit: implications for the genesis of Mesoproterozoic iron mineralization. Ore Geol. Rev. 139, 104574.
Song, W.L., Xu, C., Smith, M.P., Chakhmouradian, A.R., Brenna, M., Kynický, J., Chen, W., Yang, Y.H., Deng, M., Tang, H.Y., 2018. Genesis of the world's largest rare earth element deposit, Bayan Obo, China: protracted mineralization evolution over ~1 b.y. Geology 46, 323–326.
Stepanov, A.S., Danyushevsky, L.V., Large, R.R., Mukherjee, I., Zhukova, I.A., 2020. Deconvolution of the composition of fine-grained pyrite in sedimentary matrix by regression of time-resolved LA-ICP-MS data. Am. Mineral. 105, 820–832.
Su, W.C., Zhang, H.T., Hu, R.Z., Ge, X., Xia, B., Chen, Y.Y., Zhu, C., 2012. Mineralogy and geochemistry of gold-bearing arsenian pyrite from the Shuiyindong Carlin-type gold deposit, Guizhou, China: implications for gold depositional processes. Mineral. Deposita 47, 653–662.
Sun, J., Zhu, X.K., Chen, Y.L., Fang, N., 2013. Iron isotopic constraints on the genesis of Bayan Obo ore deposit, Inner Mongolia, China. Precambrian Res. 235, 88–106.
Sun, S.S., McDonough, W.F., 1989. Chemical and isotopic systematics of oceanic basalts: implications for mantle composition and processes. Geol. Soc. London Spec. Publ. 42, 313–345.
Tang, C.W., Zhu, H.P., 2008. The geochemical characters and genesis of trace-elements in epithermal minerals from the Xinkangmao gold deposit. Mineral. Petrol. 12, 64–70 in Chinese with English abstract.
Tang, K.D., 1990. Tectonic Development of Paleozoic Foldbelts at the North Margin of the Sino-Korean Craton. Tectonics 9, 249–260.
Tang, L., Wagner, T., Fusswinkel, T., Zhang, S.T., Xu, B., Jia, L.H., Hu, X.K., 2021. Magmatic-hydrothermal evolution of an unusual Mo-rich carbonatite: a case study using LA-ICP-MS fluid inclusion microanalysis and He–Ar isotopes from the Huangshui'an deposit, Qinling, China. Mineral. Deposita 56, 1133–1150.
Tanner, D., Henley, R.W., Mavrogenes, J.A., Holden, P., 2016. Sulfur isotope and trace element systematics of zoned pyrite crystals from the El Indio Au-Cu-Ag deposit, Chile. Contrib. Mineral. Petrol. 171, 33.
Ustundag, Z., Ustundag, I., Kadioglu, Y.K., 2007. Multi-element analysis of pyrite ores X-ray fluorescence using polarized energy-dispersive spectrometry. Appl. Radiat. Isot. 65, 809–813.
Wang, J., Tatsumoto, M., Li, X., Premo, W.R., Chao, E.C.T., 1994. A precise ^{232}Th-^{208}Pb chronology of fine grained monazite: age of the Bayan Obo REE-Fe-Nb ore deposit, China. Geochim. Cosmochim. Acta 58, 3155–3169.
Wang, K.Y., Fan, H.R., Yang, K.F., Hu, F.F., Wu, C.M., Hu, F.Y., 2010. Calcite-dolomite geothermometry of Bayan Obo carbonatites. Acta Petrol. Sin. 26, 1141–1149 in Chinese with English abstract.
Wang, K.Y., Yang, K.F., Fan, H.R., Hu, F.F., Hu, F.Y., 2012. Addressing some problems on research of the Bayan Obo deposit. Acta Geol. Sin. 86, 687–699 in Chinese with English abstract.
Wang, W.Y., Gao, J.G., Nong, Y.X., Chen, X.B., 2017. Rare earth elements and trace element geochemical of Lulu lead-zinc deposit in Luquan County, Yunnan Province. J. Chin. Soc. Rare Earths 35, 418–430 in Chinese with English abstract.

Woodhead, J.D., Harmon, R.S., Fraser, D.G., 1987. O, S, Sr, and Pb isotope variations in volcanic rocks from the Northern Mariana Islands: implications for crustal recycling in intra-oceanic arcs. Earth Planet. Sci. Lett. 83, 39–52.

Wilson, S.A., Ridley, W.I., Koenig, A.E., 2002. Development of sulfide calibration standards for the laser ablation inductively-coupled plasma mass spectrometry technique. J. Anal. At. Spectrom. 17, 406–409.

Xiao, W.J., Windley, B.F., Hao, J., Zhai, M.G., 2003. Accretion leading to collision and the Permian Solonker suture, Inner Mongolia, China: Termination of the central Asian orogenic belt. Tectonics 22. https://doi.org/10.1029/2002tc001484.

Yang, K.F., Fan, H.R., Hu, F.F., Li, X.H., Liu, J.Y., Zhao, Y.G., Liu, S., Wang, K.Y., 2007. Skarnization age in the giant Bayan Obo REE-Nb-Fe ore district, Inner Mongolia, China: Rb-Sr isochrone dating on single-grain phlogopite. Acta Petrol. Sin. 23, 1018–1022 in Chinese with English abstract.

Yang, K.F., Fan, H.R., Hu, F.F., Wang, K.Y., 2012. Sediment source of Bayan Obo Marginal rift and genesis of ore-bearing dolomite of the giant REE deposit. Acta Geolo. Sin. 86, 775–784 in Chinese with English abstract.

Yang, K.F., Fan, H.R., Pirajno, F., Li, X.C., 2019. The Bayan Obo (China) giant REE accumulation conundrum elucidated by intense magmatic differentiation of carbonatite. Geology 47, 1198–1202.

Yang, K.F., Fan, H.R., Santosh, M., Hu, F.F., Wang, K.Y., 2011. Mesoproterozoic carbonatitic magmatism in the Bayan Obo deposit, Inner Mongolia, North China: Constraints for the mechanism of super accumulation of rare earth elements. Ore Geol. Rev. 40, 122–131.

Yang, X.Y., Lai, X.D., Pirajno, F., Liu, Y.L., Ling, M.X., Sun, W.D., 2017. Genesis of the Bayan Obo Fe-REE-Nb formation in Inner Mongolia, North China Craton: a perspective review. Precambrian Res. 288, 39–71.

Yang, X.Y., Sun, W.D., Zhang, Y.X., Zheng, Y.F., 2009. Geochemical constraints on the genesis of the Bayan Obo Fe-Nb-REE deposit in Inner Mongolia, China. Geochim. Cosmochim. Acta 73, 1417–1435.

Zhang, S.H., Zhao, Y., Liu, Y., 2017. A precise zircon Th-Pb age of carbonatite sills from the world's largest Bayan Obo deposit: Implications for timing and genesis of REE-Nb mineralization. Precambrian Res. 291, 202–219.

Zhang, W., Hu, Z.C., Liu, Y.S., 2020. Iso-Compass: new freeware software for isotopic data reduction of LA-MC-ICP-MS. J. Anal. At. Spectrom. 35, 1087–1096.

Zhang, Y., Gu, X.X., Zhang, Y.M., Cheng, W.B., Sun, Y.Q., 2012. Geochemical characteristics of rare earth elements and its significance in the mineralization of quartz and pyrite in the Liubeigou gold deposit, Inner Mongolia. Bull. Mineral. Petrol. Geochem. 31, 23–30 in Chinese with English abstract.

Zhang, Z.Q., Yuan, Z.X., Tang, S.H., Bai, G., Wang, J.H., 2003. Age and Geochemistry of the Bayan Obo Ore Deposit: Geological Publishing House, Beijing, pp. 1–205 (in Chinese with English Abstract).

Zhao, K.D., Jiang, S.Y., 2007. Rare earth element and yttrium analyses of sulfides from the Dachang Sn-polymetallic ore field, Guangxi Province, China: Implication for ore genesis. Geochem. J. 41, 121–134.

Zheng, J., Yu, D.L., Yang, Z.Q., 2010. A study on the trace element geochemical characteristics of pyrite and arsenopyrite in Bake gold deposit, east Guizhou province, China. Acta Mineral. Sin. 30, 107–114 in Chinese with English abstract.

Zheng, Y., Zhang, L., Chen, Y.J., Hollings, P., Chen, H.Y., 2013. Metamorphosed Pb-Zn-(Ag) ores of the Keketale VMS deposit, NW China: Evidence from ore textures, fluid inclusions, geochronology and pyrite compositions. Ore Geol. Rev. 54, 167–180.

Zheng, Y.F., 1990. S isotope fractionation in magmatic systems: models of Rayleigh distillation and selective flux. Chin. J. Geochem. 9, 27–45.

Zheng, Y.F., 2001. Theoretical modeling of stable isotope system and its applications to geochemistry of hydrothermal ore deposits. Miner. Depos. 20, 57–70 in Chinese with English abstract.

Zhong, Y., Zhai, M.G., Peng, P., Santosh, M., Ma, X.D., 2015. Detrital zircon U-Pb dating and whole-rock geochemistry from the clastic rocks in the northern marginal basin of the North China Craton: Constraints on depositional age and provenance of the Bayan Obo Group. Precambrian Res. 258, 133–145.

Zhou, Z.G., Hu, M.M., Wu, C., Wang, G.S., Liu, C.F., Cai, A.R., Jiang, T., 2018. Coupled U-Pb dating and Hf isotopic analysis of detrital zircons from Bayan Obo Group in Inner Mongolia: Constraints on the evolution of the Bayan Obo rift belt. Geol. J. 53, 2649–2664.

Zhu, X.K., Sun, J., Pan, C., 2015. Sm-Nd isotopic constraints on rare-earth mineralization in the Bayan Obo ore deposit, Inner Mongolia, China. Ore Geol. Rev. 64, 543–553.